Millimeter-Wave Beam Selection in Time-Varying Channels With User Orientation Changes

Ashok Kumar Reddy Chavva, *Senior Member, IEEE*, and Neelesh B. Mehta, *Fellow, IEEE*

Abstract—The use of many narrow beams to overcome the adverse propagation conditions in millimeter-wave channels leads to large training durations and overheads in 5G systems. This causes the beam measurements to become outdated by different extents at the time the transmit and receive beams are selected. The rapid changes in user device orientation exacerbate this problem. We first present a novel modified bivariate Nakagami-m (MBN) model to tractably and accurately characterize the joint, non-stationary statistics of the channel gains seen at the times of measurement and data transmission. We then derive a novel and optimal beam selection rule that maximizes the average rate of the system. We use the MBN model to propose a near-optimal, practically amenable bound-based selection (PABS) rule. Our approach captures several pertinent aspects about the spatial channel model and 5G, such as transmission of periodic bursts of reference signals, feedback from the user to enable the base station to select its transmit beam, and the faster pace of updating the data rate compared to the transmit-receive beam pair. The PABS rule markedly outperforms the widely used conventional power-based selection rule and is less sensitive to user orientation changes.

Index Terms—Millimeter-wave, 5G, beamforming, antenna array, spatial channel model, beam selection, beam management, beam measurement, orientation change.

I. INTRODUCTION

IN THE quest to provide higher throughputs and accommodate a large number of mobile devices, 5G cellular communication technology has moved towards millimeter-wave bands with large bandwidths [1]–[3]. However, communication in these bands is subject to severe propagation loss, attenuation from atmospheric gases and precipitation, line-of-sight (LoS) blockage and scattering, and diffraction [4].

Beamforming with antenna arrays helps address these challenges [5]. The small wavelength facilitates antenna arrays with a large number of antennas at both base station (BS) and user equipment (UE). Large antenna arrays result in narrow beams with large array gains, which compensates for the severe propagation loss. However, narrow beams require

accurate alignment [6]. The number of transmit-receive beam pairs required to cover the full angular space in elevation and azimuth also increases.

In order to enable the UE to estimate the channel gain on each transmit-receive beam pair, the BS periodically sends reference signals on its transmit beams. For example, in the 5G new radio (NR) standard, synchronization signal blocks (SSBs) are periodically transmitted by the BS [6]–[8]. The UE uses the SSBs for initial beam acquisition. Subsequently, for beam tracking and selection during the connected mode, it uses the channel-state information reference signal (CSI-RS) along with the SSBs. The BS transmits the SSBs from all its transmit beams in an SSB burst of duration 5 milliseconds (ms). Thus, in an SSB burst, the UE can measure the gains from all the transmit beams to one of its receive beams. To estimate all the transmit-receive beam pair gains, multiple bursts are required – one for each UE receive beam. These bursts are transmitted with a period that ranges from 5 ms to 160 ms. Thus, beam acquisition can take a considerable amount of time. Therefore, the difference between the time of transmission of the reference signal and the time at which the beam pair is selected depends on the beam pair. Consequently, channel estimates obtained for different beam pairs are outdated by different extents in a time-varying environment.

In the connected mode, this process also requires the UE to report its beam measurements periodically to the BS. Using these measurements, the BS reselects the transmit beam and transmits data on it. In addition, the UE periodically feeds back channel quality information (CQI), which enables the BS to adjust its modulation and coding scheme (MCS) and data rate. This is done at a rate faster than that at which the beam measurements are fed back [8].

The change in the UE device orientation relative to the serving BS poses another new challenge [9]–[12]. Typical user movements can change the device orientation at a rate that ranges from $60°$/s to $110°$/s. In gaming scenarios, it can even go up to $800°$/s [13]. This happens even in nomadic, low mobility environments. Not only does it exacerbate the time variations in the channel, it also leads to beam misalignment, which causes a change in the mean power of the serving transmit-receive beam gain and a non-stationary channel. This requires frequent beam selection and orientation tracking as the link quality would degrade rapidly otherwise.

Given the importance of beamforming and beam selection, a considerable amount of literature has appeared on it. In [14], [15], exhaustive search is considered. The UE sequentially measures all beam pairs to select the one that

maximizes the signal-to-noise-ratio (SNR) [14], [15]. In [16], a two-step iterative beam search method is discussed. The BS sends reference signals using wide beams in the first step and then using narrow beams in the second step. In 5G NR, the UE selects the beam that maximizes the SNR [6]. In [17], beam selection is based on the signal-to-interference-plus-noise-ratio (SINR) and reference signal received power measured at both UE and BS. In [18], the angle of arrival (AoA) is estimated and the beam is tracked by measuring the received signal at specific pre-defined perturbations to the beam pattern. Capacity-based beam selection methods are presented for multiple-input-multiple-output (MIMO) channels in [19]. In [20], the users are separated into interfering and non-interfering users. First, the non-interfering users are assigned beams and then the interfering users.

In [21], the LoS and non-LoS (NLoS) paths are used to estimate the position of the UE and then select the beam. The approach in [22] trains the same transmit-receive beam pair multiple times to improve the received signal powers in specific directions and maximize the probability of tracking the beam pair that is aligned. In [23], a technique for obtaining high resolution AoA and angle of departure (AoD) estimates using wide beams is proposed. The beam is then oriented in the estimated direction. Multi-armed bandit-based approaches are used for beam selection in [24], [25].

In the above papers on beam selection [6], [14]–[16], [19], [21] and in [26], which studies dual-connectivity, the beam or beam pair with the highest SNR or measured signal power is selected. We shall refer to this as the *conventional power-based selection (CPBS)* rule. However, the CPBS rule does not account for the time-varying nature of the channel and the fact that channel measurements of different beams are outdated by different extents. While [24], [25] consider time-varying channels, only NLoS paths are considered without a model for measurement and data transmission in [24] and a numerical ray-tracing method is used in [25].

A. Focus and Contributions

In this paper, we consider the problem of beam selection in channels with time variations that occur due to user mobility and user orientation changes. The latter makes the beam gain a non-stationary random process. Our model captures several pertinent aspects about 5G NR, such as the transmission of periodic bursts of reference signals to enable beam pair measurements, feedback from the UE to enable the BS to select its transmit beam, and the faster pace at which the data rate is adapted compared to the transmit-receive beam pair. It also captures several salient aspects of the comprehensive spatial channel model (SCM), which has been used in 5G NR system design and evaluation [27]–[29]. This includes AoA, AoD, antenna geometry, LoS and NLoS paths, clusters and multiple paths per cluster, and user orientation. We make the following contributions:

- We propose a modified bivariate Nakagami-m (MBN) model to characterize in an analytically tractable manner the joint statistics of the beam gains seen at the times of measurement and data transmission. It accurately

models our observation that the beam gains at two time instants can be non-negatively or negatively correlated. For non-negative correlations, the MBN model is the bivariate Nakagami-m model [30, Ch. 6]. For negative correlations, it is based on an affine transformation of the above bivariate model. To the best of our knowledge, only the marginal Nakagami-m probability density function (PDF) has been used to model millimeter-wave channels in the literature [31], [32]. Neither the bivariate model nor its modification have been used or numerically verified for accuracy.

- We derive a novel and optimal beam selection rule that maximizes the average rate of the system when the beam pair is selected periodically on the basis of the aforementioned channel estimates that are outdated by different extents. We then use the MBN model to propose a practically amenable bound-based selection (PABS) rule that is computationally much simpler to implement.

- For channel traces generated from SCM, we show that the average rate achieved by the PABS rule is very close to that of the non-causal genie-aided rule in which the BS knows at the time of selection the gains of all the beam pairs in the future time instants. The PABS rule performs much better than the widely assumed CPBS rule, and is less sensitive to changes in the user orientation.

B. Organization and Notations

Section II presents the system model. In Section III, we propose the MBN model and verify its accuracy. We present the optimal beam selection rule and the PABS rule in Section IV. Section V contains numerical results, and is followed by our conclusions in Section VI.

Notations: We denote the PDF and cumulative distribution function (CDF) of a random variable (RV) X by $f_X(\cdot)$ and $F_X(\cdot)$, respectively. Similarly, the conditional PDF and CDF conditioned on an event A are denoted by $f_X(\cdot|A)$ and $F_X(\cdot|A)$, respectively. The expectation with respect to an RV X is denoted by $\mathbb{E}_X[\cdot]$ and the expectation conditioned on an event A by $\mathbb{E}_X[\cdot|A]$. The covariance of RVs X and Y is denoted by $\text{Cov}(X, Y)$, variance of RV X by $\text{Var}(X)$, transpose by $(\cdot)^T$, Hermitian transpose by $(\cdot)^\dagger$, real part by $\Re\{\cdot\}$, and derivative of a function f as f'.

II. SYSTEM MODEL

We consider a millimeter-wave system with a BS and a UE. The BS is equipped with a uniform linear array (ULA) that consists of N_{tx} antennas. It can transmit one beam from among B_{BS} fixed directional beams in the azimuth direction. Similarly, the UE is equipped with a ULA that consists of N_{rx} antennas. It can receive on one beam from among B_{UE} fixed directional beams in the azimuth direction. Let $\mathcal{B}_{\text{BS}} = \{1, \ldots, B_{\text{BS}}\}$ and $\mathcal{B}_{\text{UE}} = \{1, \ldots, B_{\text{UE}}\}$ denote the set of transmit beams at the BS and the set of receive beams at the UE, respectively.

A. Spatial Channel Model

Let $\psi(t)$ be the orientation of the UE with respect to the antenna array at time t. The MIMO channel matrix

$\mathbf{H}(t, \psi(t)) \in \mathcal{C}^{N_{\text{rx}} \times N_{\text{tx}}}$ between the BS and the UE at time t, which also depends on $\psi(t)$, is given by [27]–[29]

$$
\begin{aligned}
\mathbf{H}(t, \psi(t)) \\
= \sqrt{\frac{K\Lambda}{K+1}} \mathbf{u}_{\text{rx}}(\theta_{\text{LoS}}^{\text{rx}} + \psi(t)) \mathbf{u}_{\text{tx}}^{\dagger}(\theta_{\text{LoS}}^{\text{tx}}) \\
+ \sqrt{\frac{\Lambda}{(K+1)L}} \sum_{c=1}^{C} \sum_{l=1}^{L} \alpha_{c,l}(t) \mathbf{u}_{\text{rx}}(\theta_{c,l}^{\text{rx}} + \psi(t)) \mathbf{u}_{\text{tx}}^{\dagger}(\theta_{c,l}^{\text{tx}}),
\end{aligned}
\tag{1}
$$

where C is the number of clusters, L is the number of paths per cluster, $\mathbf{u}_{\text{rx}}(\cdot)$ is the array response at the receiver, $\mathbf{u}_{\text{tx}}(\cdot)$ is the array response at the transmitter, K is the Rician factor, $\theta_{c,l}^{\text{tx}}$ and $\theta_{c,l}^{\text{rx}}$ are the AoD at the BS relative to its ULA and AoA at the UE relative to its ULA, respectively, for the lth path in the cth cluster, $\theta_{\text{LoS}}^{\text{tx}}$ is the LoS AoD, $\theta_{\text{LoS}}^{\text{rx}}$ is the LoS AoA, and Λ is the path-loss. For a ULA, $\mathbf{u}_{\text{rx}}(\cdot)$ and $\mathbf{u}_{\text{tx}}(\cdot)$ are given by

$$
\mathbf{u}_{\text{rx}}(\theta) = \frac{1}{\sqrt{N_{\text{rx}}}} \left[1, e^{-j2\pi\mu^{\text{rx}}(\theta)}, \ldots, e^{-j2\pi(N_{\text{rx}}-1)\mu^{\text{rx}}(\theta)} \right]^{T}, \tag{2}
$$

$$
\mathbf{u}_{\text{tx}}(\theta) = \frac{1}{\sqrt{N_{\text{tx}}}} \left[1, e^{-j2\pi\mu^{\text{tx}}(\theta)}, \ldots, e^{-j2\pi(N_{\text{tx}}-1)\mu^{\text{tx}}(\theta)} \right]^{T}, \tag{3}
$$

where $\mu^{\text{tx}}(\theta) = d_{\text{tx}} \cos(\theta)/\lambda$, d_{tx} is the antenna spacing at the transmitter, and λ is the wavelength. Similarly, $\mu^{\text{rx}}(\theta) = d_{\text{rx}} \cos(\theta)/\lambda$ and d_{rx} is the antenna spacing at the receiver. Lastly, $\alpha_{c,l}(t) = \bar{\alpha}_{c,l} \exp(j2\pi f_D t \cos(\omega_{c,l}))$, where $f_D = v/\lambda$ is the maximum Doppler shift, v is the speed of the UE that moves at an angle θ_v, $\omega_{c,l} = \theta_{c,l}^{\text{rx}} - \theta_v + \psi(t)$, $\bar{\alpha}_{c,l}$ is a circularly symmetric complex Gaussian RV with zero mean and variance γ_c, and γ_c is the relative power of the cth cluster. The system model is illustrated in Figure 1.

Let $g_{i,p}(t)$ denote the gain between the ith transmit beam of the BS and the pth receive beam of the UE at time t. It is given by

$$
g_{i,p}(t) = |(\mathbf{v}_p^{\text{rx}})^{\dagger} \mathbf{H}(t, \psi(t)) \mathbf{v}_i^{\text{tx}}|, \tag{4}
$$

where $\mathbf{v}_i^{\text{tx}} = \mathbf{u}_{\text{tx}}(\theta_i^{\text{tx}})$ is the beamforming vector of the ith transmit beam that points in the direction θ_i^{tx} and $\mathbf{v}_p^{\text{rx}} = \mathbf{u}_{\text{rx}}(\theta_p^{\text{rx}})$ is the beamforming vector of the pth receive beam that points in the direction θ_p^{rx}. The transmit beam directions are set as $\theta_i^{\text{tx}} = (i-1)\pi/B_{\text{BS}}$, for $1 \le i \le B_{\text{BS}}$, and the receive beam directions as $\theta_p^{\text{rx}} = (p-1)\pi/B_{\text{UE}}$, for $1 \le p \le B_{\text{UE}}$.

Note: $\psi(t)$ can model any type of orientation change; it is not dependent on v. As per SCM, the number of clusters and paths, AoAs, and AoDs do not change over several measurement cycles [27]–[29]. This is because they change at a much slower timescale than that at which the MIMO channel and beam gains change.

B. SCM Statistical Parameters

The AoA $\theta_{c,l}^{\text{rx}}$ of path l of cluster c is a Gaussian RV that is wrapped over an interval of 2π radians. Its PDF $f_c^{\text{rx}}(\theta)$ is given by [28]

$$
f_c^{\text{rx}}(\theta) = \frac{1}{\sqrt{2\pi}\sigma_{\text{AoA},c}} \sum_{\ell=-\infty}^{\infty} \exp\left(\frac{-(\theta + 2\pi\ell - \bar{\theta}_{\text{AoA},c})^2}{2\sigma_{\text{AoA},c}^2} \right),
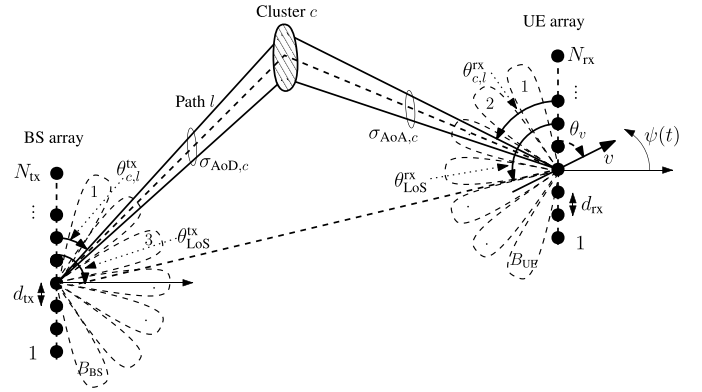$$
$$
\text{for } -\pi < \theta \le \pi. \tag{5}
$$

Fig. 1. System model: BS with N_{tx} antennas that can form one among B_{BS} beams and the UE with N_{rx} antennas that can form B_{UE} beams. Also shown is the UE orientation $\psi(t)$, speed v, and SCM.

With a slight abuse of terminology, we shall refer to $\bar{\theta}_{\text{AoA},c}$ and $\sigma_{AoA,c}$ as the mean and standard deviation, respectively, of $\theta_{c,l}^{\text{rx}}$. Similarly, the AoD $\theta_{c,l}^{\text{tx}}$ is a wrapped Gaussian RV with mean $\bar{\theta}_{\text{AoD},c}$ and standard deviation $\sigma_{\text{AoD},c}$. Its PDF is denoted by $f_c^{\text{tx}}(\theta)$. In SCM, $\sigma_{\text{AoA},c}$ and $\sigma_{AoD,c}$ are themselves exponential RVs with means ξ_{AoA} and ξ_{AoD}, respectively [28], [29].

C. Beam Measurement and Data Transmission Model

The beam measurement and data transmission take place over beam measurement cycles, each of duration T_{meas}. A cycle consists of three phases that overlap in time, namely, beam measurement, beam selection, and data transmission. In the beam measurement phase, the BS transmits pilot bursts from different transmit beams. In the beam selection phase, the UE selects the receive beam and the BS selects the transmit beam. In the data transmission phase, the BS transmits data using its serving beam $\tilde{i}$ and the UE receives using its serving beam $\tilde{p}$.

In order to explore the trade-off between measuring more beam pairs and the increased sensitivity to time-variations in the gains due to the extra time this takes, we study two models for beam measurements. The first one is called full measurement cycle (FMC). In it, the BS transmits B_{UE} bursts so that the UE can measure all the $B_{\text{UE}}B_{\text{BS}}$ beam pairs. This is similar to the models of [6], [16], [33]. The second one is called partial measurement cycle (PMC). In it, the UE measures different subsets of the beam pairs in different measurement cycles.

1) Beam Measurements: In a pilot burst, the BS transmits pilot symbols from its B_{BS} beams one after the other in a burst of duration T_{p}, while the UE receives from one of its receive beams. The pilot bursts are spaced T_{m} apart in time.

FMC: Each beam measurement cycle consists of B_{UE} pilot bursts and is of duration $B_{\text{UE}}T_{\text{m}}$. In the first pilot burst, the UE measures the gains from all the B_{BS} transmit beams to its first receive beam. It, thus, measures the beam pairs $(1,1), (2,1), \ldots, (B_{\text{BS}}, 1)$, where the tuple (i,p) represents the beam pair that consists of transmit beam i and receive beam p. In the second pilot burst, the UE receives from its second receive beam and measures the beam pairs $(1,2), (2,2), \ldots, (B_{\text{BS}}, 2)$, and so on. After B_{UE}
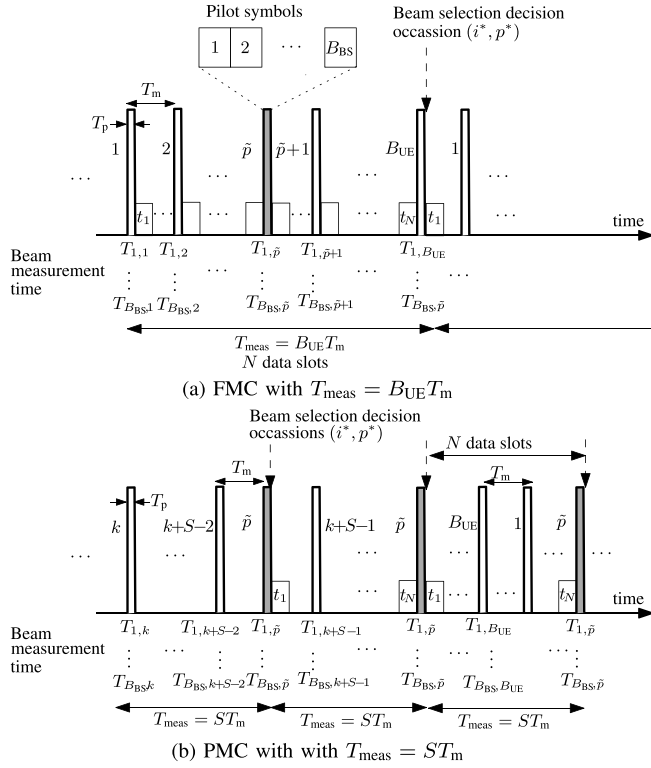
Fig. 2. Measurement, selection, and data transmission model: Beam selection occurs once in a beam measurement cycle, which is of duration T_{meas}. Every pilot burst of duration T_p consists of B_{BS} pilot symbols, one each from B_{BS} transmit beams from the BS. There are N data slots in a beam measurement cycle.

pilot bursts, the UE has measured all the $B_{\text{UE}} B_{\text{BS}}$ beam pairs. FMC is illustrated in Figure 2a.

PMC: Each beam measurement cycle consists of $S < B_{\text{UE}}$ pilot bursts. Therefore, its duration is ST_{m}. Let the UE receive the first pilot burst on beam k. It, thus, measures the beam pairs $(1, k), (2, k), \ldots, (B_{\text{BS}}, k)$. It receives the second pilot burst on beam $(k + 1)$ and measures the beam pairs $(1, k + 1), (2, k + 1), \ldots, (B_{\text{BS}}, k + 1)$. It does this for $(S - 1)$ pilot bursts. In the last (S^{th}) pilot burst, the UE receives with its serving beam $\tilde{p}$ and measures the beam pairs $(1, \tilde{p}), (2, \tilde{p}), \ldots, (B_{\text{BS}}, \tilde{p})$. This enables the UE to obtain fresh estimates for its serving receive beam, which has higher odds of being reselected in a slowly-varying environment. Thus, the UE measures the gains using its receive beams $k, k + 1, \ldots, k + S - 2, \tilde{p}$ in the measurement cycle.[1] In the next measurement cycle, the UE measures the gains using the receive beams $k + S - 1, k + S, \ldots$. PMC is illustrated in Figure 2b.

In general, let the UE measure the beam pair (i, p) at time $T_{i,p}$ and let the corresponding gain be $g_{i,p}(T_{i,p})$. Let the vector $\mathbf{g} = [g_{1,1}(T_{1,1}), \ldots, g_{i,p}(T_{i,p}), \ldots, g_{B_{\text{BS}}, B_{\text{UE}}}(T_{B_{\text{BS}}, B_{\text{UE}}})]$ represent the most recent beam measurements of the $B_{\text{BS}} B_{\text{UE}}$ beam pairs. These span multiple measurement cycles in PMC.

---

[1] In case $\tilde{p} \in \{k, k + 1, \ldots, k + S - 2\}$, then the UE moves to the next receive beam and skips receiving using $\tilde{p}$, which it will receive with in the last pilot burst in the measurement cycle.

2) Beam Selection: At the end of each measurement cycle, the UE selects the beam pair (i^*, p^*) on the basis of $\mathbf{g}$, and reports the transmit beam i^* to the BS using its serving beam pair $(\tilde{i}, \tilde{p})$. Then, (i^*, p^*) becomes the serving beam pair in the next measurement cycle. The beam selection feedback delay and the time required by the hardware to switch to the selected beams at the BS and the UE are assumed to be small compared to the time taken to measure the many beams [6], [8]. Thus, the BS can switch its transmit beam with a periodicity of ST_{m}.

3) Data Transmission: It consists of N slots, each of duration T_{slot}. These span the entire measurement cycle, as do the pilot bursts. Slot n starts at time t_n. At the beginning of every slot, the UE feeds back to the BS the rate at which it can receive data in that slot. This model captures the fact that in 5G NR, the BS can adapt its data rate multiple times with the same beam pair [6], [8]. The gain variations within a slot are negligible since because T_{slot} is small compared to the coherence time of the channel. Then, as per Shannon's capacity formula, the rate $R(g_{i^*, p^*}(t))$ in bits/s/Hz on the selected beam pair is given by

$$R(g_{i^*, p^*}(t)) = \log_2\left(1 + \frac{P_{\text{tx}} g_{i^*, p^*}^2(t)}{\sigma^2}\right), \qquad (6)$$

where P_{tx} is the transmit power and σ^2 is the noise variance.

Note: To ensure tractability, we do not explicitly model the variations in $\mathbf{H}(t, \psi(t))$ due to LoS blockage. Our approach applies so long as the time taken to measure all the beam pairs is smaller than the average duration for which a blockage remains unchanged.

III. MBN Model for Time-Varying Channels of SCM

To design the beam selection rule, we first develop an analytically tractable model for the joint statistics of the gains $g_{i,p}(t)$ and $g_{i,p}(t + \tau)$ obtained from SCM, where τ is the time lag. We characterize them statistically using the Nakagami-m distribution since it is known to accurately model the channel measurements obtained from several propagation scenarios [28], [31], [32], [34]. It subsumes NLoS Rayleigh fading and accurately approximates LoS Rician fading.

Consider first the case when these gains are non-negatively correlated. We propose modeling their joint PDF using the bivariate Nakagami-m model. As per it, the bivariate PDF of $g_{i,p}(t)$ and $g_{i,p}(t + \tau)$ is given by [30, (6.1)]

$$
\begin{aligned}
&f_{g_{i,p}(t), g_{i,p}(t+\tau)}(r_1, r_2) \\
&= \frac{4m^{m+1} r_1^m r_2^m (\Omega_{i,p}(t) \Omega_{i,p}(t+\tau))^{-\frac{m+1}{2}}}{\Gamma(m)[1 - \delta_{i,p}(t, t+\tau)](\delta_{i,p}(t, t+\tau))^{\frac{m-1}{2}}} \\
&\quad \times \exp\left[\frac{-m}{1 - \delta_{i,p}(t, t+\tau)}\left(\frac{r_1^2}{\Omega_{i,p}(t)} + \frac{r_2^2}{\Omega_{i,p}(t+\tau)}\right)\right] \\
&\quad \times I_{m-1}\left(\frac{2mr_1 r_2 \sqrt{\delta_{i,p}(t, t+\tau)}}{\sqrt{\Omega_{i,p}(t)} \Omega_{i,p}(t+\tau)[1 - \delta_{i,p}(t, t+\tau)]}\right),
\end{aligned}
$$
$$(7)$$

where m is the Nakagami parameter, $\Omega_{i,p}(t)$ is the mean channel power at measurement time t, $\delta_{i,p}(t, t+\tau) \geq 0$ is the

power correlation coefficient, and $I_m(.)$ denotes the modified Bessel function of the first kind with order m [35, (9.6.19)]. To the best of our knowledge, the bivariate Nakagami-m PDF for modeling the time-varying channels of SCM and capturing the effect of user orientation changes has not been employed in the millimeter-wave literature, nor has its accuracy been verified.

A. Expressions for Bivariate Nakagami-m Parameters

We now derive $\Omega_{i,p}(t)$, $\delta_{i,p}(t, t+\tau)$, and m in (7) in terms of the SCM parameters.

The pth receive beam gain $Z_p^{\text{rx}}(\theta) = \left(\mathbf{v}_p^{\text{rx}}\right)^\dagger \mathbf{u}_{\text{rx}}(\theta)$ in the direction θ is given by

$$Z_p^{\text{rx}}(\theta) = \frac{1}{N_{\text{rx}}} \exp\left(-j(N_{\text{rx}}-1)\pi\left[\mu^{\text{rx}}(\theta) - \mu^{\text{rx}}\left(\theta_p^{\text{rx}}\right)\right]\right) \times \frac{\sin\left(N_{\text{rx}}\pi\left[\mu^{\text{rx}}(\theta) - \mu^{\text{rx}}\left(\theta_p^{\text{rx}}\right)\right]\right)}{\sin\left(\pi\left[\mu^{\text{rx}}(\theta) - \mu^{\text{rx}}\left(\theta_p^{\text{rx}}\right)\right]\right)}. \quad (8)$$

It follows that

$$\left|Z_p^{\text{rx}}(\theta)\right|^2 = \frac{1}{N_{\text{rx}}^2} \frac{\sin^2\left(N_{\text{rx}}\pi\left[\mu^{\text{rx}}(\theta) - \mu^{\text{rx}}\left(\theta_p^{\text{rx}}\right)\right]\right)}{\sin^2\left(\pi\left[\mu^{\text{rx}}(\theta) - \mu^{\text{rx}}\left(\theta_p^{\text{rx}}\right)\right]\right)}. \quad (9)$$

Similarly, for the ith transmit beam gain $Z_i^{\text{tx}}(\theta) = \left(\mathbf{v}_i^{\text{tx}}\right)^\dagger \mathbf{u}_{\text{tx}}(\theta)$ in the direction θ, we have

$$\left|Z_i^{\text{tx}}(\theta)\right|^2 = \frac{1}{N_{\text{tx}}^2} \frac{\sin^2\left(N_{\text{tx}}\pi\left[\mu^{\text{tx}}(\theta) - \mu^{\text{tx}}\left(\theta_i^{\text{tx}}\right)\right]\right)}{\sin^2\left(\pi\left[\mu^{\text{tx}}(\theta) - \mu^{\text{tx}}\left(\theta_i^{\text{tx}}\right)\right]\right)}. \quad (10)$$

1) Mean Channel Power $\Omega_{i,p}(t)$: As shown in Appendix A, $\Omega_{i,p}(t) = \mathbb{E}\left[g_{i,p}^2(t)\right]$ is given by

$$\Omega_{i,p}(t) = \frac{\Lambda}{K+1}\sum_{c=1}^{C}\gamma_c \bar{G}_{p,c}^{\text{rx}}(t)\bar{G}_{i,c}^{\text{tx}}(t) + \frac{K\Lambda}{K+1}\left|Z_p^{\text{rx}}\left(\theta_{\text{LoS}}^{\text{rx}} + \psi(t)\right)\right|^2 \left|Z_i^{\text{tx}}\left(\theta_{\text{LoS}}^{\text{tx}}\right)\right|^2, \quad (11)$$

where $Z_p^{\text{rx}}(\cdot)$ and $Z_i^{\text{tx}}(\cdot)$ are given above,

$$\bar{G}_{p,c}^{\text{rx}}(t) = \frac{1}{\sqrt{\pi}}\sum_{q=1}^{N_{\text{GH}}} w_q \left|Z_p^{\text{rx}}\left(\sqrt{2}\sigma_{\text{AoA},c}x_q + \bar{\theta}_{\text{AoA},c} + \psi(t)\right)\right|^2, \quad (12)$$

$$\bar{G}_{i,c}^{\text{tx}}(t) = \frac{1}{\sqrt{\pi}}\sum_{q=1}^{N_{\text{GH}}} w_q \left|Z_i^{\text{tx}}\left(\sqrt{2}\sigma_{\text{AoD},c}x_q + \bar{\theta}_{\text{AoD},c}\right)\right|^2, \quad (13)$$

w_q and x_q are the qth Gauss-Hermite (GH) weight and abscissa, respectively, and N_{GH} is the GH integration order [35, (25.4.46)].

2) Power Correlation Coefficient $\delta_{i,p}(t, t+\tau)$: It is defined as

$$\delta_{i,p}(t, t+\tau) \triangleq \frac{\mathbb{E}\left[g_{i,p}^2(t)g_{i,p}^2(t+\tau)\right] - \Omega_{i,p}(t)\Omega_{i,p}(t+\tau)}{\sqrt{\text{Var}(g_{i,p}^2(t))\text{Var}(g_{i,p}^2(t+\tau))}}. \quad (14)$$

This general definition is applicable to non-stationary processes. The term

$$\text{Var}(g_{i,p}^2(t)) \triangleq \mathbb{E}\left[g_{i,p}^4(t)\right] - \Omega_{i,p}^2(t),$$

in the denominator is derived in Appendix B. It equals

$$\text{Var}(g_{i,p}^2(t)) = \frac{2\Lambda^2}{L(K+1)^2}\left(\sum_{c_1=1}^{C}\gamma_{c_1}^2 F_{p,c_1}^{\text{rx}}(t)F_{i,c_1}^{\text{tx}}(t)\right.$$

$$+2(L-1)\sum_{c_1=1}^{C}\gamma_{c_1}^2\left(\bar{G}_{p,c_1}^{\text{rx}}(t)\right)^2\left(\bar{G}_{i,c_1}^{\text{tx}}(t)\right)^2$$

$$+2L\left[\sum_{c_1=1}^{C}\gamma_{c_1}\bar{G}_{p,c_1}^{\text{rx}}(t)\bar{G}_{i,c_1}^{\text{tx}}(t)\right]$$

$$\left.\times\sum_{c_2=1,c_2\neq c_1}^{C}\gamma_{c_2}\bar{G}_{p,c_2}^{\text{rx}}(t)\bar{G}_{i,c_2}^{\text{tx}}(t)\right)$$

$$+\frac{2K\Lambda^2\left|Z_p^{\text{rx}}\left(\theta_{\text{LoS}}^{\text{rx}} + \psi(t)\right)\right|^2\left|Z_i^{\text{tx}}\left(\theta_{\text{LoS}}^{\text{tx}}\right)\right|^2}{(K+1)^2}$$

$$\times\sum_{c_1=1}^{C}\gamma_{c_1}\bar{G}_{p,c_1}^{\text{rx}}(t)\bar{G}_{i,c_1}^{\text{tx}}(t), \quad (15)$$

where

$$F_{p,c}^{\text{rx}}(t) = \frac{1}{\sqrt{\pi}}\sum_{q=1}^{N_{\text{GH}}} w_q \left|Z_p^{\text{rx}}\left(\sqrt{2}\sigma_{\text{AoA},c}x_q + \bar{\theta}_{\text{AoA},c} + \psi(t)\right)\right|^4, \quad (16)$$

$$F_{i,c}^{\text{tx}}(t) = \frac{1}{\sqrt{\pi}}\sum_{q=1}^{N_{\text{GH}}} w_q \left|Z_i^{\text{tx}}\left(\sqrt{2}\sigma_{\text{AoD},c}x_q + \bar{\theta}_{\text{AoD},c}\right)\right|^4. \quad (17)$$

The term $\mathbb{E}\left[g_{i,p}^2(t)g_{i,p}^2(t+\tau)\right]$ in the numerator is also derived in Appendix B. It equals

$$\mathbb{E}\left[g_{i,p}^2(t)g_{i,p}^2(t+\tau)\right] = T_{i,p}^{\text{NLoS}}(t,\tau) + T_{i,p}^{\text{LoS}}(t,\tau) + T_{i,p}^{\text{LoS,NLoS}}(t,\tau). \quad (18)$$

Here, $T_{i,p}^{\text{NLoS}}(t,\tau)$ captures cross-products involving the NLoS terms, and is given by (19) at the bottom of the next page.

$T_{i,p}^{\text{LoS}}(t,\tau)$ captures cross-products involving the LoS terms, and is given by

$$T_{i,p}^{\text{LoS}}(t,\tau) = \frac{K^2\Lambda^2}{(K+1)^2}\left|Z_p^{\text{rx}}\left(\theta_{\text{LoS}}^{\text{rx}} + \psi(t)\right)\right|^2 \times \left|Z_p^{\text{rx}}\left(\theta_{\text{LoS}}^{\text{rx}} + \psi(t+\tau)\right)\right|^2\left|Z_i^{\text{tx}}\left(\theta_{\text{LoS}}^{\text{tx}}\right)\right|^4. \quad (21)$$

$T_{i,p}^{\text{LoS,NLoS}}(t,\tau)$ captures cross-products involving the LoS and NLoS terms, and is given by

$$T_{i,p}^{\text{LoS,NLoS}}(t,\tau)$$

$$= \frac{K\Lambda^2\left|Z_i^{\text{tx}}\left(\theta_{\text{LoS}}^{\text{tx}}\right)\right|^2}{(K+1)^2}$$

$$\times\left[\left(\sum_{c=1}^{C}\gamma_c\bar{G}_{p,c}^{\text{rx}}(t)\bar{G}_{i,c}^{\text{tx}}(t)\right)\left|Z_p^{\text{rx}}\left(\theta_{\text{LoS}}^{\text{rx}} + \psi(t+\tau)\right)\right|^2\right.$$

$$+\left(\sum_{c=1}^{C}\gamma_c\bar{G}_{p,c}^{\text{rx}}(t+\tau)\bar{G}_{i,c}^{\text{tx}}(t)\right)\left|Z_p^{\text{rx}}\left(\theta_{\text{LoS}}^{\text{rx}} + \psi(t)\right)\right|^2$$

$$+2\Re\left\{\left(\sum_{c=1}^{C}\gamma_c\Theta_c^{\text{rx}}(t,\tau)\bar{G}_{i,c}^{\text{tx}}(t)\right)\right.$$

$$\left.\left.\times\left(Z_p^{\text{rx}}\left(\theta_{\text{LoS}}^{\text{rx}} + \psi(t)\right)\right)^* Z_p^{\text{rx}}\left(\theta_{\text{LoS}}^{\text{rx}} + \psi(t+\tau)\right)\right\}\right]. \quad (22)$$

We see that $\delta_{i,p}(t, t+\tau)$ is dependent on user orientation and speed, and also the SCM parameters such as θ_v, λ, d_{tx}, d_{rx}, N_{tx}, N_{rx}, C, γ_c, $\theta^{\text{tx}}_{\text{LoS}}$, and $\theta^{\text{rx}}_{\text{LoS}}$.

3) Nakagami Parameter m: We choose m as its maximum likelihood estimate at time t. It is given by [36]

$$m = \frac{\Omega^2_{i,p}(t)}{\text{Var}(g^2_{i,p}(t))}, \qquad (23)$$

where $\Omega_{i,p}(t)$ is given in (11) and $\text{Var}(g^2_{i,p}(t))$ is given in (15).

B. Modeling Negative Power Correlation

As mentioned, $g_{i,p}(t)$ and $g_{i,p}(t+\tau)$ can be negatively correlated, in which case $\delta_{i,p}(t, t+\tau) < 0$. To understand this, Figure 3 plots the level-set contours of the empirical bivariate PDF of $g_{i,p}(t)/\sqrt{\Omega_{i,p}(t)}$ and $g_{i,p}(t+\tau)/\sqrt{\Omega_{i,p}(t+\tau)}$ at $t = 20$ ms for $\tau = 17$ ms and 23 ms at which $\delta_{i,p}(t, t+\tau)$ are -0.83 and 0.81, respectively. The correlation coefficients have approximately the same absolute value but opposite signs. The contours are generated from $100,000$ traces of the gains of all the beam pairs for $B_{\text{BS}} = 18$, $B_{\text{UE}} = 18$, $N_{\text{tx}} = N_{\text{rx}} = 20$, $d_{\text{rx}} = d_{\text{tx}} = 0.25\lambda$, $v = 3.85$ kmph, and a carrier frequency of 28 GHz [5]. This corresponds to a maximum Doppler shift of 100 Hz. Each trace consists of 120 samples that are spaced 1 ms apart. The SCM parameters are $K = 3$, $\xi_{\text{AoD}} = 10.2°$, $\xi_{\text{AoD}} = 15.5°$, $C = 4$, $L = 20$, and $\theta_v = 90°$, and the UE orientation change rate is $\psi'(t) = 60°/s$ [27], [28]. We make the following observation:

Numerical Observation 1: The level-set contours for non-negative power correlation coefficients are concentric, and so are those for negative power correlation coefficients.
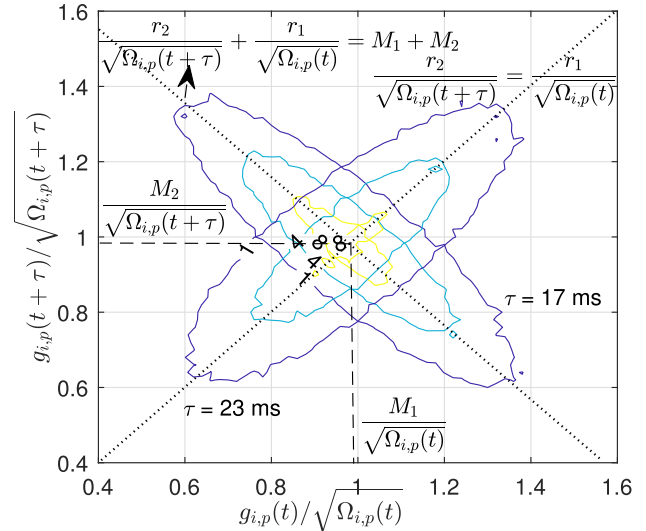

Fig. 3. Level-set contour plot of the empirical bivariate PDF of $g_{i,p}(t)/\sqrt{\Omega_{i,p}(t)}$ and $g_{i,p}(t+\tau)/\sqrt{\Omega_{i,p}(t+\tau)}$ for $\tau = 17$ ms and 23 ms with $\delta_{i,p}(t, t+\tau) = -0.83$ and 0.81, respectively, at $\psi'(t) = 60°/s$ ($K = 3$, $\xi_{\text{AoD}} = 10.2°$, $\xi_{\text{AoA}} = 15.5°$, $C = 4$, and $L = 20$, $t = 20$ ms). The PDF $f_{g_{i,p}(t),g_{i,p}(t+\tau)}(r_1, r_2)$ levels are 1, 4, and 8.

Furthermore, all the level-set contours share the same center $(M_1/\sqrt{\Omega_{i,p}(t)}, M_2/\sqrt{\Omega_{i,p}(t+\tau)})$.

Expression for (M_1, M_2): It is the point at which the bivariate Nakagami-m PDF peaks. In general, from (7), (M_1, M_2) is the solution of the following two equations:

$$\frac{\partial}{\partial r_1} f_{g_{i,p}(t),g_{i,p}(t+\tau)}(r_1, r_2)$$
$$= m(1 - 2\kappa_1 r_1^2) + \kappa_2 r_1 r_2 \frac{I'_{m-1}(\kappa_2 r_1 r_2)}{I_{m-1}(\kappa_2 r_1 r_2)} = 0, \quad (24)$$

$$T^{\text{NLoS}}_{i,p}(t, \tau) = \frac{\Lambda^2}{L(K+1)^2}\left[2\sum_{c_1=1}^{C}\gamma^2_{c_1}\bar{G}^{\text{rx}}_{p,c_1}(t)F^{\text{tx}}_{i,c_1}(t)\bar{G}^{\text{rx}}_{p,c_1}(t+\tau)\right.$$

$$+L\left[\sum_{c_1=1}^{C}\gamma_{c_1}\bar{G}^{\text{rx}}_{p,c_1}(t)\bar{G}^{\text{tx}}_{i,c_1}(t)\right]\sum_{c_2=1,c_2\neq c_1}^{C}\gamma_{c_2}\bar{G}^{\text{rx}}_{p,c_2}(t+\tau)\bar{G}^{\text{tx}}_{i,c_2}(t)$$

$$+(L-1)\sum_{c_1=1}^{C}\gamma^2_{c_1}\bar{G}^{\text{rx}}_{p,c_1}(t)\left(\bar{G}^{\text{tx}}_{i,c_1}(t)\right)^2\bar{G}^{\text{rx}}_{p,c_1}(t+\tau)$$

$$+L\left[\sum_{c_1=1}^{C}\gamma_{c_1}\Theta^{\text{rx}}_{c_1}(t,\tau)\bar{G}^{\text{tx}}_{i,c_1}(t)\right]\sum_{c_2=1,c_2\neq c_1}^{C}\gamma_{c_2}\left(\Theta^{\text{rx}}_{c_2}(t,\tau)\right)^*\bar{G}^{\text{tx}}_{i,c_2}(t)$$

$$+(L-1)\sum_{c_1=1}^{C}\gamma^2_{c_1}\Theta^{\text{rx}}_{c_1}(t,\tau)\left(\bar{G}^{\text{tx}}_{i,c_1}(t)\right)^2\left(\Theta^{\text{rx}}_{c_1}(t,\tau)\right)^*\right], \qquad (19)$$

where

$$\Theta^{\text{rx}}_c(t,\tau) = \sum_{q=1}^{N_{\text{GH}}}\frac{w_q}{\sqrt{\pi}}Z^{\text{rx}}_p\left(\sqrt{2}\sigma_{\text{AoA},c}x_q + \bar{\theta}_{\text{AoA},c} + \psi(t)\right)\left(Z^{\text{rx}}_p\left(\sqrt{2}\sigma_{\text{AoA},c}x_q + \bar{\theta}_{\text{AoA},c} + \psi(t+\tau)\right)\right)^*$$

$$\times \exp\left(4\pi jtf_D\sin\left(\sqrt{2}\sigma_{\text{AoA},c}x_q + \bar{\theta}_{\text{AoA},c} + \frac{\psi(t) + \psi(t+\tau)}{2} - \theta_v\right)\sin\left(\frac{\psi(t+\tau) - \psi(t)}{2}\right)\right)$$

$$\times \exp\left(-2\pi j\tau f_D\cos\left(\sqrt{2}\sigma_{\text{AoA},c}x_q + \bar{\theta}_{\text{AoA},c} + \psi(t+\tau) - \theta_v\right)\right). \qquad (20)$$
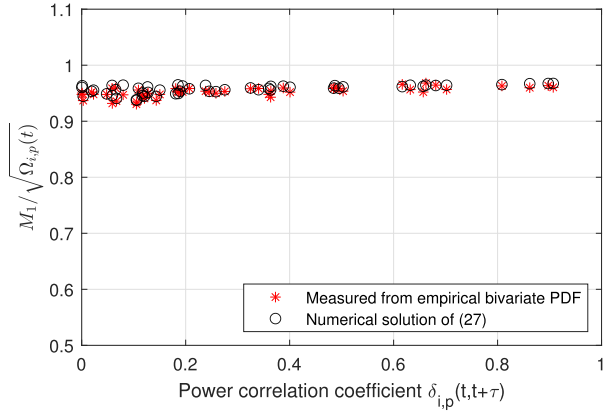
Fig. 4. Comparison of solution of (26) and the value of $M_1/\sqrt{\Omega_{i,p}(t)}$ measured from the empirical bivariate PDF ($t = 0$ ms, $\psi'(t) = 60°$/s, $K = 3$, $\xi_{\text{AoD}} = 10.2°$, $\xi_{\text{AoA}} = 15.5°$, $C = 4$, and $L = 20$).

$$\frac{\partial}{\partial r_2} f_{g_{i,p}(t),g_{i,p}(t+\tau)}(r_1, r_2)$$

$$= m(1 - 2\kappa_3 r_2^2) + \kappa_2 r_1 r_2 \frac{I'_{m-1}(\kappa_2 r_1 r_2)}{I_{m-1}(\kappa_2 r_1 r_2)} = 0, \quad (25)$$

where $\kappa_1 = 1/([1 - \delta_{i,p}(t,t+\tau)]\Omega_{i,p}(t))$, $\kappa_2 = \frac{2m\sqrt{\delta_{i,p}(t,t+\tau)}}{\sqrt{\Omega_{i,p}(t)\Omega_{i,p}(t+\tau)(1-\delta_{i,p}(t,t+\tau))}}$, and $\kappa_3 = ([1 - \delta_{i,p}(t,t+\tau)]\Omega_{i,p}(t+\tau))^{-1}$. Eliminating common terms yields $M_1/\sqrt{\Omega_{i,p}(t)} = M_2/\sqrt{\Omega_{i,p}(t+\tau)}$. Substituting this in (24), it follows that M_1 is the solution of the following non-linear equation:

$$m(1 - 2\kappa_1 r_1^2) + \kappa_2 \sqrt{\frac{\Omega_{i,p}(t+\tau)}{\Omega_{i,p}(t)}} \frac{I'_{m-1}\left(\sqrt{\frac{\Omega_{i,p}(t+\tau)}{\Omega_{i,p}(t)}} r_1^2\right)}{I_{m-1}\left(\sqrt{\frac{\Omega_{i,p}(t+\tau)}{\Omega_{i,p}(t)}} r_1^2\right)} r_1^2 = 0.$$
$$(26)$$

To the best of our knowledge, no closed-form expression is known for it. The only exception is $\delta_{i,p}(t,t+\tau) = 0$, i.e., $g_{i,p}(t)$ and $g_{i,p}(t+\tau)$ are mutually independent. Then, M_1 is the value of r_1 at which the marginal Nakagami-m PDF $f_{g_{i,p}(t)}(r_1)$ is maximized, and M_2 is the value of r_2 at which $f_{g_{i,p}(t+\tau)}(r_2)$ is maximized. They can be shown to be [34]

$$M_1 = \sqrt{\frac{(2m-1)\Omega_{i,p}(t)}{2m}} \text{ and } M_2 = \sqrt{\frac{(2m-1)\Omega_{i,p}(t+\tau)}{2m}}.$$
$$(27)$$

Since no closed-form solution is known for (26), we study it numerically. Figure 4 plots $M_1/\sqrt{\Omega_{i,p}(t)}$ as a function of $\delta_{i,p}(t,t+\tau)$.[2] The simulation parameters are the same as those for Figure 3. It leads to the following observation.

Numerical Observation 2: M_1 and M_2 are approximated with small error by (27) for all $\delta_{i,p}(t,t+\tau) \geq 0$.

Figure 3 also leads to the following observation.

Numerical Observation 3: The major axes of the level-set contours for the non-negative and negative power correlation coefficients are perpendicular to each other.

The above observations apply to other parameter settings as well; results for these are not shown due to space constraints.

[2]The corresponding results for M_2 are similar. We do not show them to conserve space.

Explanation and Implications: $f_{g_{i,p}(t),g_{i,p}(t+\tau)}(r_1, r_2)$ in (7) is a symmetric function of the variables $r_1/\sqrt{\Omega_{i,p}(t)}$ and $r_2/\sqrt{\Omega_{i,p}(t+\tau)}$. This symmetry coupled with the fact that the correlation coefficient is non-negative implies that the major axis of the contours is a $45°$-line with a positive slope of 1. Any other positive slope would render the bivariate PDF asymmetric. From Numerical Observation 2, it also passes through the point $\left(\sqrt{\frac{2m-1}{2m}}, \sqrt{\frac{2m-1}{2m}}\right)$ since the marginal Nakagami-m PDF, when subject to the above scaling of $\sqrt{\Omega_{i,p}(t)}$, is maximized at $\sqrt{\frac{2m-1}{2m}}$.

For a negative correlation coefficient, we expect the bivariate PDF to remain a symmetric function of $r_1/\sqrt{\Omega_{i,p}(t)}$ and $r_2/\sqrt{\Omega_{i,p}(t+\tau_1)}$. Using the same reasoning as above, this implies that the major axis is now a $135°$-line with a negative slope of -1 that passes through the point $\left(\sqrt{\frac{2m-1}{2m}}, \sqrt{\frac{2m-1}{2m}}\right)$. As above, any other angle would imply that the bivariate PDF for the negative correlation coefficient is not a symmetric function of $r_1/\sqrt{\Omega_{i,p}(t)}$ and $r_2/\sqrt{\Omega_{i,p}(t+\tau_1)}$. Therefore, the major axis of the level-set contours for the negative correlation coefficient is perpendicular to the line $r_2/\sqrt{\Omega_{i,p}(t+\tau)} = r_1/\sqrt{\Omega_{i,p}(t)}$. Since it passes through $(M_1/\sqrt{\Omega_{i,p}(t)}, M_2/\sqrt{\Omega_{i,p}(t+\tau)})$, which is given in (27), it can be shown to be given by the line

$$\frac{r_2}{\sqrt{\Omega_{i,p}(t+\tau)}} = \sqrt{\frac{(2m-1)\Omega_{i,p}(t)}{2m}}\left(1 + \frac{\Omega_{i,p}(t)}{\Omega_{i,p}(t+\tau)}\right)$$
$$- \frac{\Omega_{i,p}(t)}{\Omega_{i,p}(t+\tau)} \frac{r_1}{\sqrt{\Omega_{i,p}(t)}}. \quad (28)$$

Based on these observations, we propose the following bivariate PDF $\tilde{f}_{g_{i,p}(t),g_{i,p}(t+\tau)}(r_1, r_2)$:

$$\tilde{f}_{g_{i,p}(t),g_{i,p}(t+\tau)}(r_1, r_2)$$

$$= \frac{4m^{m+1}(a-r_1)^m r_2^m [\Omega_{i,p}(t)\Omega_{i,p}(t+\tau)]^{-\frac{m+1}{2}}}{\zeta(m, 2(2m-1))(1-\rho)\rho^{\frac{m-1}{2}}}$$

$$\times \exp\left[\frac{-m}{1-\rho}\left(\frac{(a-r_1)^2}{\Omega_{i,p}(t)} + \frac{r_2^2}{\Omega_{i,p}(t+\tau)}\right)\right]$$

$$\times I_{m-1}\left(\frac{2m\sqrt{\rho}(a-r_1)r_2}{\sqrt{\Omega_{i,p}(t))\Omega_{i,p}(t+\tau)}(1-\rho)}\right),$$

for $0 \leq r_1 \leq a, r_2 \geq 0$, $\quad (29)$

where $a = \sqrt{2(2m-1)\Omega_{i,p}(t)/m}$, $\zeta(\cdot, \cdot)$ is the incomplete gamma function [37, (8.350.1)], and $\rho > 0$ is a parameter that models correlation.

Rationale: The PDF in (29) is obtained by the following sequence of transformations of RVs that are designed to satisfy the above observations. First, consider the normalized RVs $Y_1 = g_{i,p}(t)/\sqrt{\Omega_{i,p}(t)}$ and $Y_2 = g_{i,p}(t+\tau)/\sqrt{\Omega_{i,p}(t)}$ with power correlation coefficient ρ. From (7), we can show that $f_{Y_1,Y_2}(y_1, y_2) = \frac{4m^{m+1}y_1^m y_2^m \exp\left[\frac{-m(y_1^2+y_2^2)}{1-\rho}\right]}{\Gamma(m)(1-\rho)\rho^{\frac{m-1}{2}}} I_{m-1}\left(\frac{2m\sqrt{\rho}y_1 y_2}{\sqrt{1-\rho}}\right)$, for $y_1, y_2 \geq 0$. To rotate this by $90°$ in the counter-clockwise direction around the point (M_1, M_2) as per Numerical Observations 1 and 3, we apply the variable transformation

$\tilde{Y}_1 = 2\sqrt{(2m-1)/(2m)} - Y_2$ and $\tilde{Y}_2 = Y_1$. Lastly, we scale back the two RVs using the transformation $g_{i,p}(t) = Y_1\sqrt{\Omega_{i,p}(t)}$ and $g_{i,p}(t+\tau) = Y_2\sqrt{\Omega_{i,p}(t+\tau)}$. This sequence of transformations yields the PDF in (29). Its support is restricted to $0 \le r_1 \le a$ and $r_2 \ge 0$ since the resultant RVs must be non-negative. This leads to the scaling factor $\zeta(m, 2(2m-1))$ appearing instead of $\Gamma(m)$ in the denominator to ensure that $f_{g_{i,p}(t), g_{i,p}(t+\tau)}(r_1, r_2)$ is a valid PDF.[3]

Intuitively, based on the above rationale, one would expect $\delta_{i,p}(t, t+\tau) \approx -\rho$. We study this below and also derive an exact expression for $\delta_{i,p}(t, t+\tau)$. As per its definition in (14), we need expressions for $\mathbb{E}\left[g_{i,p}^2(t) g_{i,p}^2(t+\tau)\right]$, $\mathbb{E}\left[g_{i,p}^4(t+\tau)\right]$, and $\mathbb{E}\left[g_{i,p}^2(t+\tau)\right]$, which determine $\mathrm{Var}\left(g_{i,p}^2(t+\tau)\right)$, and $\mathbb{E}\left[g_{i,p}^4(t)\right]$ and $\mathbb{E}\left[g_{i,p}^2(t)\right]$, which determine $\mathrm{Var}\left(g_{i,p}^2(t)\right)$. From (29), they are as follows. The finite support in (29) makes them involved. We skip the steps to save space.

$$
\begin{aligned}
&\mathbb{E}\left[g_{i,p}^2(t)\right] \\
&= \frac{\Omega_{i,p}(t)}{m\zeta(m, 2(2m-1))}\Bigg[2(2m-1) \\
&\quad \times \zeta(m, 2(2m-1)) + \zeta(m+1, 2(2m-1)) \\
&\quad -2\sqrt{2(2m-1)}\zeta\left(m+\frac{1}{2}, 2(2m-1)\right)\Bigg],
\end{aligned}
\tag{30}
$$

$$
\begin{aligned}
&\mathbb{E}\left[g_{i,p}^4(t)\right] \\
&= \frac{\Omega_{i,p}^2(t)}{m^2\zeta(m, 2(2m-1))}\Bigg[(41m^2 - 27m + 4) \\
&\quad \times \zeta(m, 2(2m-1)) - 2\sqrt{2(2m-1)}(10m-3) \\
&\quad \times \zeta\left(m+\frac{1}{2}, 2(2m-1)\right)\Bigg],
\end{aligned}
\tag{31}
$$

$$
\begin{aligned}
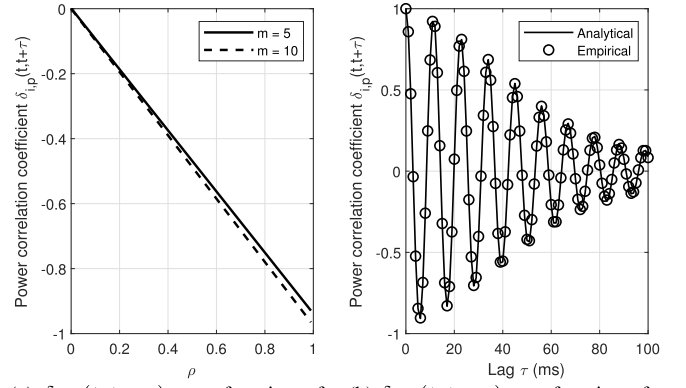&\mathbb{E}\left[g_{i,p}^2(t+\tau)\right] \\
&= \frac{\Omega_{i,p}(t+\tau)(1-\rho)^{m+1}}{m\zeta(m, 2(2m-1))} \\
&\quad \times \sum_{k=0}^{\infty} \frac{\rho^k \zeta\left(k+m, \frac{2(2m-1)}{1-\rho}\right)\Gamma(m+k+1)}{k!\Gamma(m+k)},
\end{aligned}
\tag{32}
$$

$$
\begin{aligned}
&\mathbb{E}\left[g_{i,p}^4(t+\tau)\right] \\
&= \frac{\Omega_{i,p}^2(t+\tau)(1-\rho)^{m+2}}{m^2\zeta(m, 2(2m-1))} \\
&\quad \times \sum_{k=0}^{\infty} \frac{\rho^k \zeta\left(k+m, \frac{2(2m-1)}{1-\rho}\right)\Gamma(m+k+2)}{k!\Gamma(m+k)},
\end{aligned}
\tag{33}
$$

and

$$
\begin{aligned}
&\mathbb{E}\left[g_{i,p}^2(t) g_{i,p}^2(t+\tau)\right] \\
&= \frac{\Omega_{i,p}(t)\,\Omega_{i,p}(t+\tau)}{m^2\zeta(m, 2(2m-1))} \\
&\quad \times \Bigg[m(5m-2+\rho)\zeta(m, 2(2m-1)) \\
&\quad -\sqrt{2(2m-1)}(2m+\rho)\zeta\left(m+\frac{1}{2}, 2(2m-1)\right)\Bigg].
\end{aligned}
\tag{34}
$$

---

[3]We have observed numerically that for negative power correlations, $g_{i,p}(t)$ seldom exceeds a. In the rare event that this happens, we clip it to a in order to comply with the support for the bivariate PDF in (29).

(a) $\delta_{i,p}(t, t+\tau)$ as a function of ρ (b) $\delta_{i,p}(t, t+\tau)$ as a function of τ in (29)

Fig. 5. MBN model: Power correlation coefficient $\delta_{i,p}(t, t+\tau)$ ($t = 20$ ms, $\psi'(t) = 60°$/s, $K = 3$, $\xi_{\mathrm{AoD}} = 10.2°$, $\xi_{\mathrm{AoA}} = 15.5°$, $C = 4$, and $L = 20$).

For $\rho = 0$, we can show that (32) and (33) simplify to

$$
\mathbb{E}\left[g_{i,p}^2(t+\tau)\right] = \Omega_{i,p}(t+\tau),
\tag{35}
$$

and

$$
\mathbb{E}\left[g_{i,p}^4(t+\tau)\right] = \Omega_{i,p}^2(t+\tau)\left(1+\frac{1}{m}\right).
\tag{36}
$$

Figure 5a plots the power correlation coefficient computed from the above expressions as a function of ρ for $m = 5$ and 10 for the SCM parameters used for Figure 3. We see that it is negative. It is close to $-\rho$ for both values of m, which reaffirms our intuition. The match improves as m increases. Therefore, we shall use $|\delta_{i,p}(t, t+\tau)|$ instead of ρ henceforth for the bivariate PDF in (29).

C. MBN Model Verification

The bivariate PDF in (7) and (29) together constitute the MBN model. To assess its accuracy, we use the same simulation parameters as those for Figure 3. Figure 5b plots the empirically measured value of $\delta_{i,p}(t, t+\tau)$ from the SCM traces and the value analytically computed from Section III-A.2 as a function of τ. We observe a good match between the analytical and empirical curves for the entire range of τ, which spans multiple coherence intervals. For $0 \le \tau < 3$ ms, the power correlation coefficient is non-negative. However, for $3 \le \tau < 9$ ms, it is negative. $\delta_{i,p}(t, t+\tau)$ exhibits a damped oscillatory behavior. The empirical values of M_1 and M_2 from Figure 3 turn out to be 0.8652 and 0.8250. They are within 1% of the values computed from (27).

To further assess the accuracy of the proposed MBN PDF, Figure 6a plots the conditional CDF $F_{g_{i,p}(t+\tau)}(x|g_{i,p}(t))$ for different values of $g_{i,p}(t)$ for $\delta_{i,p}(t, t+\tau) = 0.81$, and Figure 6b does the same for $\delta_{i,p}(t, t+\tau) = -0.83$. These are measured from the channel traces generated above. We observe a good match over a three orders of magnitude range between the empirically obtained conditional CDF and the one derived from the bivariate PDFs in (7) and (29). In Figure 6a, $F_{g_{i,p}(t+\tau)}(x|g_{i,p}(t))$ shifts to the right as $g_{i,p}(t)$ increases because $\delta_{i,p}(t, t+\tau)$ is positive. On the other hand, in Figure 6b, $F_{g_{i,p}(t+\tau)}(x|g_{i,p}(t))$ shifts to the left as $g_{i,p}(t)$
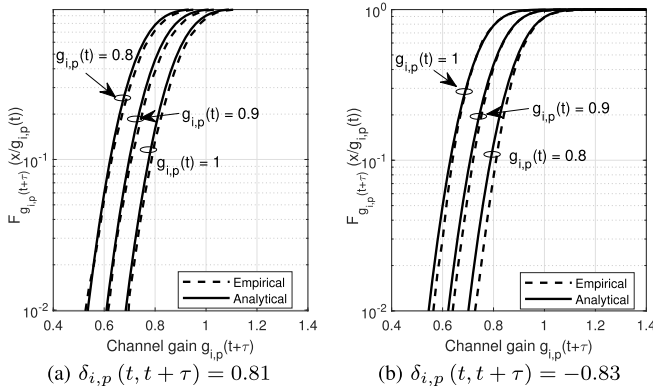
Fig. 6. MBN model verification: Conditional CDF $F_{g_{i,p}(t+\tau)}(x|g_{i,p}(t))$ for non-negative and negative power correlation coefficients ($t = 20$ ms, $\psi'(t) = 60°/$s, $K = 3$, $\xi_{\text{AoD}} = 10.2°$, $\xi_{\text{AoA}} = 15.5°$, $C = 4$, and $L = 20$).

increases because $\delta_{i,p}(t, t+\tau)$ is negative. To keep the notation simple, we denote $\delta_{i,p}(T_{i,p}, t)$ by $\rho_{i,p}(t)$ henceforth.

IV. RATE-OPTIMAL BEAM SELECTION

A beam selection rule $\Phi: (\mathbb{R}^+)^{B_{\text{BS}}} \times (\mathbb{R}^+)^{B_{\text{UE}}} \rightarrow \{(1,1), \ldots, (B_{\text{BS}}, B_{\text{UE}})\}$ is a mapping from $B_{\text{BS}}B_{\text{UE}}$ measurements to a beam pair (i, p). Our objective is to find the rule that maximizes the average data rate over the N data slots of a beam measurement cycle given the beam measurements $\mathbf{g}$. The data rate is adapted in every slot. In the kth slot, it is $R(g_{i,p}(t_k))$ and its average is $\mathbb{E}_{\mathbf{g}, g_{i,p}(t_k)}[R(g_{i,p}(t_k))]$. The optimization problem is as follows:

$$\max_{\Phi}\left\{\frac{1}{N}\sum_{k=1}^{N}\mathbb{E}_{\mathbf{g}, g_{i,p}(t_k)}[R(g_{i,p}(t_k))]\right\}, \quad (37)$$

$$\text{s.t. } (i, p) = \Phi(\mathbf{g}). \quad (38)$$

Its solution is as follows.

Result 1: The optimal selection rule selects the beam pair (i^*, p^*) that is given by

$$(i^*, p^*)$$
$$= \underset{i \in \mathcal{B}_{\text{BS}}, p \in \mathcal{B}_{\text{UE}}}{\arg\max}\left\{\frac{1}{N}\sum_{k=1}^{N}\mathbb{E}_{g_{i,p}(t_k)}\left[R(g_{i,p}(t_k))\,\big|\,g_{i,p}(T_{i,p})\right]\right\}. \quad (39)$$

Proof: The proof is given in Appendix C. ∎

Thus, the beam pair (i, p) that has the highest average data rate over the N slots conditioned on its beam measurement $g_{i,p}(T_{i,p})$ is optimal. From (7) and (29), the conditional expectations in (39) turn out to be single integrals. The UE needs to compute them numerically for each value of $g_{i,p}(t)$. To reduce this computational burden, we present a simpler rule below.

Since $R(.)$ is a concave function, applying the Jensen's inequality [37, (12.411)], we get

$$\frac{1}{N}\sum_{k=1}^{N}\mathbb{E}_{g_{i,p}(t_k)}\left[R(g_{i,p}(t_k))\,\big|\,g_{i,p}(T_{i,p})\right]$$
$$\leq \frac{1}{N}\sum_{k=1}^{N}\log_2\left(1 + \frac{P_{\text{tx}}d_{i,p}(t_k)}{\sigma^2}\right), \quad (40)$$

where $d_{i,p}(t)$ is called the *selection metric* and equals

$$d_{i,p}(t) = \mathbb{E}_{g_{i,p}(t)}\left[g_{i,p}^2(t)\,\Big|\,g_{i,p}(T_{i,p})\right]. \quad (41)$$

The expression for $d_{i,p}(t)$ can be derived in closed-form from the MBN model as follows:

a) $\rho_{i,p}(t) \geq 0$*:* From (7), we can show that the conditional PDF $f_{g_{i,p}(t)}(r_2|g_{i,p}(T_{i,p}) = r_1)$ is

$$f_{g_{i,p}(t)}(r_2|g_{i,p}(T_{i,p}) = r_1)$$
$$= \frac{2mr_2^m}{r_1^{m-1}\Omega_{i,p}(t)[1-\rho_{i,p}(t)]}\left(\frac{\Omega_{i,p}(T_{i,p})}{\rho_{i,p}(t)\Omega_{i,p}(t)}\right)^{\frac{m-1}{2}}$$
$$\times \exp\left(-\frac{m\rho_{i,p}(t)r_1^2}{[1-\rho_{i,p}(t)]\Omega_{i,p}(T_{i,p})} - \frac{mr_2^2}{[1-\rho_{i,p}(t)]\Omega_{i,p}(t)}\right)$$
$$\times I_{m-1}\left(\frac{2m\sqrt{\rho_{i,p}(t)}r_1r_2}{[1-\rho_{i,p}(t)]\sqrt{\Omega_{i,p}(T_{i,p})\Omega_{i,p}(t)}}\right). \quad (42)$$

Using (42) and the identity $\int_0^\infty r_2^{m+2}e^{-dr_2^2}I_{m-1}(\nu r_2)\,dr_2 = e^{-\frac{\nu^2}{4d}}\frac{\nu^{m-1}(\nu^2+4dm)}{(2\,d)^{m+2}}$ [37, (6.631.1)] to evaluate the conditional expectation in (41), we get the following closed-form expression:

$$d_{i,p}(t) = \frac{\Omega_{i,p}(t)}{\Omega_{i,p}(T_{i,p})}\Big[(1 - \rho_{i,p}(t))\Omega_{i,p}(T_{i,p})$$
$$+ \rho_{i,p}(t)g_{i,p}^2(T_{i,p})\Big]. \quad (43)$$

b) $\rho_{i,p}(t) < 0$*:* Along similar lines as above, from the bivariate PDF in (29), we can show after algebraic manipulations that $f_{g_{i,p}(t)}(r_2|g_{i,p}(T_{i,p}) = r_1)$ has a form similar to (42) except that r_1 is replaced with $(a - r_1)$. Substituting it in (41) and simplifying further yields

$$d_{i,p}(t) = \frac{\Omega_{i,p}(t)}{\Omega_{i,p}(T_{i,p})}\Bigg[(1 - |\rho_{i,p}(t)|)\Omega_{i,p}(T_{i,p})$$
$$+ |\rho_{i,p}(t)|(a - g_{i,p}(T_{i,p}))^2\Bigg]. \quad (44)$$

PABS Rule: Using the above results, we propose the following rule for all correlations:

$$(i^*, p^*) = \underset{i \in \mathcal{B}_{\text{BS}}, p \in \mathcal{B}_{\text{UE}}}{\arg\max}\left\{\frac{1}{N}\sum_{k=1}^{N}\log_2\left(1 + \frac{P_{\text{tx}}d_{i,p}(t_k)}{\sigma^2}\right)\right\}. \quad (45)$$

For $\rho_{i,p}(t) \geq 0$, $d_{i,p}(t)$ is a linear combination of the mean channel power $\Omega_{i,p}(t)$ and the beam measurement $g_{i,p}^2(T_{i,p})$. When $g_{i,p}(T_{i,p})$ is large, the odds that the beam pair (i, p) is selected increase. While, for $\rho_{i,p}(t) < 0$, the reverse is true. As $|\rho_{i,p}(t)|$ decreases from 1 to 0, the weightage for the term that depends on $g_{i,p}(T_{i,p})$ decreases. Another point to note from (11) is that $\Omega_{i,p}(t)$ is a function of the orientation $\psi(t)$ of the UE. The selection rule, thus, takes into account the change in the user's orientation in each of the N slots. We also note that the PABS rule is different from the following widely used CPBS rule [6], [14]–[16], [19]:

$$(i^*, p^*) = \underset{i \in \mathcal{B}_{\text{BS}}, p \in \mathcal{B}_{\text{UE}}}{\arg\max}\left\{g_{i,p}^2(T_{i,p})\right\}. \quad (46)$$

To implement the PABS rule, the UE needs to know its orientation $\psi(t)$ and speed so that it can compute $\rho_{i,p}(t)$ and $\Omega_{i,p}(t)$. The UE can estimate $\psi(t)$ using orientation sensors, which are now available commercially [9]–[12], [38]. Similarly, the UE can estimate its speed from the level-crossing rate or the channel covariance [39]. Alternately, the UE can directly measure $\rho_{i,p}(t)$ and $\Omega_{i,p}(t)$ from previous beam gain estimates. However, in practice, the number of samples used for this purpose needs to be chosen carefully to balance statistical accuracy and the ability of the system to react to changes in the channel parameters. Note that the BS does not need to know these parameters.

V. NUMERICAL RESULTS AND PERFORMANCE BENCHMARKING

We now present Monte Carlo simulation results that quantify the effect of different system parameters such as UE speed, number of paths and paths per cluster, transmit and receive ULA parameters, and measurement model related parameters. A new aspect that we also explore is the effect of the UE orientation change rate $\psi'(t)$ on the performance.

Simulation Setup: We illustrate the results for $B_{BS} = 18$, $B_{UE} = 18$, $N_{tx} = N_{rx} = 40$, $d_{rx} = d_{tx} = 0.25\lambda$, $v = 3.85$ kmph, and a carrier frequency of 28 GHz [5]. Let $\eta = G_{max}^{tx} G_{max}^{rx} P_{tx}\Lambda/\sigma^2$ denote the peak SNR when the transmit and receive beams are aligned, where $G_{max}^{tx} = 16$ dB and $G_{max}^{rx} = 16$ dB represent the peak transmit and receive beam gains, respectively. For SCM, the parameters are $K = 3$, $\xi_{AoD} = 10.2°$, $\xi_{AoA} = 15.5°$, $C = 4$, and $L = 20$ [28]. The beam measurement and data transmission parameters are $T_{slot} = 0.125$ ms and $T_p = 5.14 T_{slot}$. For example, when $S = 6$ and $T_m = 20$ ms, the beam measurement cycle duration is $T_{meas} = 120$ ms. Using (1) we generate 30 SCM channel traces, each of duration 12 s, for a given value of $\psi'(t)$. The MBN model is used only for calculating the metric as per (45) and selecting the beam.[4] We then compute the rate averaged over all the traces.

Benchmarking: We benchmark the PABS rule with the following rules:
- *CPBS [6], [14]–[16], [19]:* It is given by (46).
- *Genie-Aided Selection Rule:* It is given by

$$(i^*, p^*) = \arg\max_{i\in\mathcal{B}_{BS},p\in\mathcal{B}_{UE}} \left\{ \sum_{k=1}^{N} \log_2\left(1 + \frac{P_{tx}g_{i,p}^2(t_k)}{\sigma^2}\right) \right\}. \quad (47)$$

This rule is non-causal because it requires the BS to know at the time of selection the gains for all the beams in the next N data slots. It provides an upper bound on the average rate achievable by any practical causal rule.

A comparison with the approaches in [18], [20]–[26] is not possible due to the differences in the measurement, CSI feedback, and data models. For example, in [18], the UE
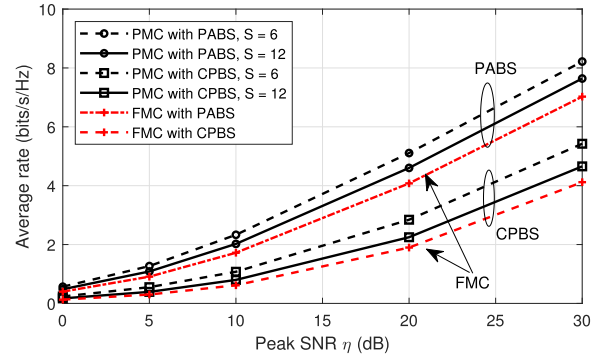

Fig. 7. Performance benchmarking of the average rates of the CPBS and PABS rules with the FMC and PMC measurement models as a function of the peak SNR η ($B_{UE} = B_{BS} = 18$, $T_m = 20$ ms, and $\psi'(t) = 60°$/s).
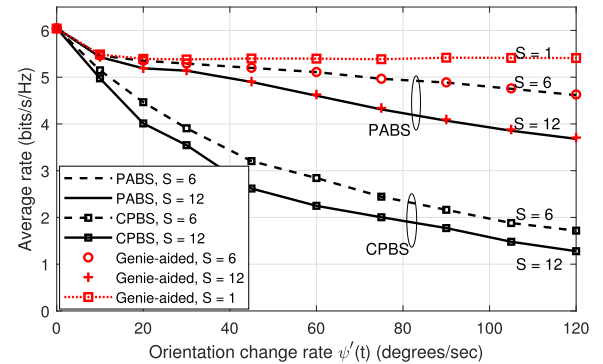

Fig. 8. Average rate as a function of the UE orientation change rate $\psi'(t)$ for PMC ($B_{UE} = B_{BS} = 18$, $T_m = 20$ ms, and $\eta = 20$ dB).

perturbs the beams to find the AoA. In [20], [26], the focus is on clustering the users spatially. Our approach is complementary to the multi-armed bandit-based methods [24], [25]. This is because the beam measurement sequence, which these methods optimize, can be modified to account for time variations and user orientation changes as per our approach.

A. Numerical Results

1) Role of Measurement Model: Figure 7 compares the average rates of the CPBS and PABS rules as a function of the peak SNR η for $\psi'(t) = 60°$/s for FMC and PMC. Consider, first, PMC. The average rate of the CPBS rule for $S = 6$ is greater than that for $S = 12$. This is because the serving beam is measured more frequently and the beam measurement cycle is shorter for $S = 6$. The same applies to the PABS rule. Another observation is that the PABS rule achieves a higher average rate than the CPBS rule. The gap between the two increases as η increases. For both rules, the average rates with PMC for $S = 6$ and 12 are more than that with FMC. Therefore, to avoid clutter, we show results for PMC henceforth.

2) Effect of UE Orientation Change Rate: Figure 8 plots the average rate as a function of the orientation change rate $\psi'(t)$ for CPBS, PABS, and the genie-aided rule for different S, which determines the measurement cycle duration. Consider, first, the CPBS rule. When $\psi'(t)$ increases from $30°$/s to $90°$/s, its average rate decreases by 44% and 50% for $S = 6$ and 12, respectively. Thus, the performance degradation is significant. As observed earlier, $S = 6$ leads to a higher average data

---

[4]To compute its parameters, we use $N_{GH} = 24$ in (12), (13), (16), and (17). To compute (20), we use $N_{GH} = 8\tau f_D$, subject to a minimum of 24 terms. It increases as τf_D increases because the number of zeroes of the function $\Theta_c^{rx}(t,\tau)$, which is oscillatory, increase. However, we cap the maximum number of terms to 63. The computed values are accurate to within 0.1%.
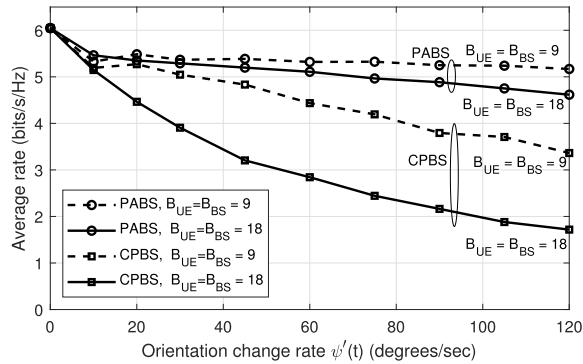
Fig. 9. Effect of beam-width: Average rate as a function of the UE orientation change rate $\psi'(t)$ for PMC ($B_{\text{UE}} = B_{\text{BS}} = 18$, $T_m = 20$ ms, and $\eta = 20$ dB).

rate than $S = 12$. On the other hand, the PABS rule is robust to changes in the UE orientation. This is because its selection metric in (45) accounts for the correlation between the channel states at the times of measurement and data transmission, and also the change in the mean channel power. The gap between the two rules markedly increases as $\psi'(t)$ increases. For example, for $S = 12$, the average rate of the PABS rule is 45% and 105% more than that of CPBS rule at $\psi'(t) = 30°$/s and $60°$/s, respectively. The average rate of the PABS rule is close to that of the genie-aided rule for both S; thus, the PABS rule is near-optimal. Even though the Jensen's bound that is used in (40) can be loose, the closeness to the genie-aided results shows that the beam that maximizes the bound often maximizes the objective function in (40). To understand the benefits from receive beam prediction, we also plot results for the genie-aided rule with $S = 1$, which measures and selects the best beam at the end of every measurement cycle. As expected, it provides an upper bound on the average rate of any beam selection rule.

3) Effect of Beam-Width: Figure 9 plots the average rate as a function of $\psi'(t)$ for CPBS, PABS, and the genie-aided rule for $S = 6$ for the following two parameter sets: 1) $N_{\text{tx}} = 40$, $N_{\text{rx}} = 40$, $B_{\text{BS}} = 18$, and $B_{\text{UE}} = 18$: This corresponds to 3-dB beam-widths of $6°$ to $12°$, and 2) $N_{\text{tx}} = 20$, $N_{\text{rx}} = 20$, $B_{\text{BS}} = 9$, and $B_{\text{UE}} = 9$: This corresponds to 3-dB beam-widths of $12°$ to $24°$. The average rates of both PABS and CPBS rules increase as the beam-width increases. This is because the serving beam can retain a larger gain for a longer portion of the measurement cycle when the beam-width is large. Furthermore, with a smaller beam-width, more time is needed to measure all the beams. As observed earlier, the average rate of the PABS rule is higher than that of the CPBS rule, and the gap between the two increases as $\psi'(t)$ increases.

VI. CONCLUSION

In a millimeter-wave beamforming system with time-varying channels and user orientation changes, the gains of the many transmit-receive beam pairs that were estimated at different times were outdated by different extents at the time the beam pair was selected. We saw that for SCM, the MBN model accurately characterized the time-evolution of the non-stationary beam gains for both non-negatively

and negatively correlated scenarios. The correlation coefficient could change signs even for the same beam pair. The MBN model was based on the bi-variate Nakagami-m PDF and an affine transformation of it. It led to a near-optimal and computationally simple PABS rule to determine the beam pair that maximized the average rate of the system over multiple slots of a measurement cycle.

The PABS rule markedly outperformed the CPBS rule and was robust to the UE orientation changes. From the genie-aided results, we observed that predicting the receive beam could improve the average rate. An interesting research avenue is characterizing the impact of imperfect CSI, transmit and receive non-idealities, and inaccurate orientation estimates.

APPENDIX

A. Derivation of Expression for Mean Channel Power $\mathbb{E}\left[|g_{i,p}(t)|^2|g_{i,p}(t+\tau)|^2\right]$

Substituting the expression for $g_{i,p}(t)$ from (4) in $\mathbb{E}\left[g_{i,p}^2(t)\right]$, using the independence of the RVs $\bar{\alpha}_{c,l}(t)$, $\theta_{c,l}^{\text{rx}}$, and $\theta_{c,l}^{\text{tx}}$, and $\mathbb{E}\left[|\bar{\alpha}_{c,l}(t)|^2\right] = \gamma_c\Lambda$, we get

$$\Omega_{i,p}(t) = \frac{1}{L(K+1)}\sum_{c=1}^{C}\sum_{l=1}^{L}\mathbb{E}\left[|\bar{\alpha}_{c,l}(t)|^2\right]$$
$$\times\mathbb{E}\left[\left|Z_p^{\text{rx}}\left(\theta_{c,l}^{\text{rx}}+\psi(t)\right)\right|^2\right]\mathbb{E}\left[\left|Z_i^{\text{tx}}\left(\theta_{c,l}^{\text{tx}}\right)\right|^2\right]$$
$$+\frac{K\Lambda}{K+1}\left|Z_p^{\text{rx}}\left(\theta_{\text{LoS}}^{\text{rx}}+\psi(t)\right)\right|^2\left|Z_i^{\text{tx}}\left(\theta_{\text{LoS}}^{\text{tx}}\right)\right|^2. \quad (48)$$

From the PDF in (5), the expectation $\bar{G}_{p,c}^{\text{rx}}(t) = \mathbb{E}\left[\left|Z_p^{\text{rx}}\left(\theta_{c,l}^{\text{rx}}+\psi(t)\right)\right|^2\right]$ is given by

$$\bar{G}_{p,c}^{\text{rx}}(t) = \frac{1}{\sqrt{2\pi}\sigma_{\text{AoA},c}}\sum_{\ell=-\infty}^{\infty}\int_{-\pi}^{\pi}\left|Z_p^{\text{rx}}\left(\theta+\psi(t)\right)\right|^2$$
$$\times\exp\left(\frac{-(\theta+2\pi\ell-\bar{\theta}_{\text{AoA},c})^2}{2\sigma_{\text{AoA},c}^2}\right)d\theta, \quad (49)$$
$$= \frac{1}{\sqrt{2\pi}\sigma_{\text{AoA},c}}\int_{-\infty}^{\infty}\left|Z_p^{\text{rx}}\left(\theta+\psi(t)\right)\right|^2$$
$$\times\exp\left(\frac{-(\theta-\bar{\theta}_{\text{AoA},c})^2}{2\sigma_{\text{AoA},c}^2}\right)d\theta. \quad (50)$$

No closed-form expression is known for (49) because of the involved form of its integrand. Therefore, to evaluate it, we use GH quadrature, as per which $\int_{-\infty}^{\infty}\exp(-x^2)f(x)dx = \sum_{1}^{N_{\text{GH}}}w_if(x_i)$ [35, (25.4.46)]. This yields (12). The expression for $\bar{G}_{i,c}^{\text{tx}}(t) = \mathbb{E}\left[\left|Z_i^{\text{tx}}\left(\theta_{c,l}^{\text{tx}}\right)\right|^2\right]$ in (13) is obtained in a similar manner. Substituting these expressions in (48) yields (11).

B. Brief Derivation of Expression for $\mathbb{E}\left[|g_{i,p}(t)|^2|g_{i,p}(t+\tau)|^2\right]$

Substituting the expression for $g_{i,p}(t)$ from (4), expanding the terms, and taking expectation yields (18), where the terms $T_{i,p}^{\text{NLoS}}(t,\tau)$, $T_{i,p}^{\text{LoS}}(t,\tau)$, and $T_{i,p}^{\text{LoS,NLoS}}(t,\tau)$ are as follows.

$T_{i,p}^{\text{NLoS}}(t,\tau)$ consists of cross-products involving the NLoS channel paths. It is given by

$$T_{i,p}^{\text{NLoS}}(t,\tau) = Q_1 + Q_2 + Q_3 + Q_4 + Q_5, \tag{51}$$

where

$$Q_1 = \frac{\Lambda^2}{L^2(K+1)^2} \sum_{c_1=1}^{C} \sum_{l_1=1}^{L} \mathbb{E}\left[|\bar{\alpha}_{c_1,l_1}(t)|^4\right]$$
$$\times \mathbb{E}\left[|Z_p^{\text{rx}}(\theta_{c_1,l_1}^{\text{rx}} + \psi(t))|^2\right] \mathbb{E}\left[|Z_i^{\text{tx}}(\theta_{c_1,l_1}^{\text{tx}})|^4\right]$$
$$\times \mathbb{E}\left[|Z_p^{\text{rx}}(\theta_{c_1,l_1}^{\text{rx}} + \psi(t+\tau))|^2\right], \tag{52}$$

$$Q_2 = \frac{\Lambda^2}{L^2(K+1)^2} \sum_{c_1=1}^{C} \left[\sum_{l_1=1}^{L} \mathbb{E}\left[|\bar{\alpha}_{c_1,l_1}(t)|^2\right] \right.$$
$$\times \mathbb{E}\left[|Z_p^{\text{rx}}(\theta_{c_1,l_1}^{\text{rx}} + \psi(t))|^2\right] \mathbb{E}\left[|Z_i^{\text{tx}}(\theta_{c_1,l_1}^{\text{tx}})|^2\right]$$
$$\times \left[\sum_{l_2=1,l_2 \neq l_1}^{L} \mathbb{E}\left[|\bar{\alpha}_{c_1,l_2}(t)|^2\right] \mathbb{E}\left[|Z_i^{\text{tx}}(\theta_{c_1,l_2}^{\text{tx}})|^2\right] \right.$$
$$\left. \left. \times \mathbb{E}\left[|Z_p^{\text{rx}}(\theta_{c_1,l_2}^{\text{rx}} + \psi(t+\tau))|^2\right] \right] \right], \tag{53}$$

$$Q_3 = \frac{\Lambda^2}{L^2(K+1)^2} \left[\sum_{c_1=1}^{C} \sum_{l_1=1}^{L} \mathbb{E}\left[|\bar{\alpha}_{c_1,l_1}(t)|^2\right] \right.$$
$$\times \mathbb{E}\left[|Z_p^{\text{rx}}(\theta_{c_1,l_1}^{\text{rx}} + \psi(t))|^2\right] \mathbb{E}\left[|Z_i^{\text{tx}}(\theta_{c_1,l_1}^{\text{tx}})|^2\right]$$
$$\times \left[\sum_{c_2=1,c_2\neq c_1}^{C} \sum_{l_2=1}^{L} \mathbb{E}\left[|\bar{\alpha}_{c_2,l_2}(t)|^2\right] \mathbb{E}\left[|Z_i^{\text{tx}}(\theta_{c_2,l_2}^{\text{tx}})|^2\right] \right.$$
$$\left. \left. \times \mathbb{E}\left[|Z_p^{\text{rx}}(\theta_{c_2,l_2}^{\text{rx}} + \psi(t+\tau))|^2\right] \right], \tag{54}$$

$$Q_4 = \frac{\Lambda^2}{L^2(K+1)^2} \left[\sum_{c_1=1}^{C} \sum_{l_1=1}^{L} \mathbb{E}\left[\alpha_{c_1,l_1}(t)\alpha_{c_1,l_1}^*(t+\tau)\right] \right.$$
$$\times Z_p^{\text{rx}}(\theta_{c_1,l_1}^{\text{rx}} + \psi(t))(Z_p^{\text{rx}}(\theta_{c_1,l_1}^{\text{rx}} + \psi(t+\tau)))^* \right]$$
$$\times \mathbb{E}\left[|Z_i^{\text{tx}}(\theta_{c_1,l_1}^{\text{tx}})|^2\right]$$
$$\times \left[\sum_{c_2=1,c_1\neq c_2}^{C} \sum_{l_2=1}^{L} \mathbb{E}\left[\alpha_{c_2,l_2}^*(t)\alpha_{c_2,l_2}(t+\tau)\right] \right.$$
$$\times (Z_p^{\text{rx}}(\theta_{c_2,l_2}^{\text{rx}} + \psi(t)))^* Z_p^{\text{rx}}(\theta_{c_2,l_2}^{\text{rx}} + \psi(t+\tau))]$$
$$\left. \times \mathbb{E}\left[|Z_i^{\text{tx}}(\theta_{c_2,l_2}^{\text{tx}})|^2\right] \right], \tag{55}$$

and

$$Q_5 = \frac{\Lambda^2}{L^2(K+1)^2} \sum_{c_1=1}^{C} \left[\sum_{l_1=1}^{L} \mathbb{E}\left[\alpha_{c_1,l_1}(t)\alpha_{c_1,l_1}^*(t+\tau)\right] \right.$$
$$\times Z_p^{\text{rx}}(\theta_{c_1,l_1}^{\text{rx}} + \psi(t))(Z_p^{\text{rx}}(\theta_{c_1,l_1}^{\text{rx}} + \psi(t+\tau)))^*$$

$$\times \mathbb{E}\left[|Z_i^{\text{tx}}(\theta_{c_1,l_1}^{\text{tx}})|^2\right] \right]$$
$$\times \left[\sum_{l_2=1,l_2\neq l_1}^{L} \mathbb{E}\left[\alpha_{c_1,l_2}^*(t)\alpha_{c_1,l_2}(t+\tau)\right] \right.$$
$$\times (Z_p^{\text{rx}}(\theta_{c_1,l_2}^{\text{rx}} + \psi(t)))^* Z_p^{\text{rx}}(\theta_{c_1,l_2}^{\text{rx}} + \psi(t+\tau))]$$
$$\left. \times \mathbb{E}\left[|Z_i^{\text{tx}}(\theta_{c_1,l_2}^{\text{tx}})|^2\right] \right]. \tag{56}$$

The many terms arise because we are computing the expectation of a fourth-order summation; many possible combinations of terms arise from the four summations.

Since $\bar{\alpha}_{c,l}(t)$ is a circularly symmetric complex Gaussian RV, we get $\mathbb{E}\left[|\bar{\alpha}_{c,l}(t)|^4\right] = 2\gamma_c^2$ and, as before, $\mathbb{E}\left[|\bar{\alpha}_{c,l}(t)|^2\right] = \gamma_c$. The expressions for the terms $\mathbb{E}\left[|Z_p^{\text{rx}}(\theta_{c,l}^{\text{rx}} + \psi(t))|^2\right] = \bar{G}_{p,c}^{\text{rx}}(t)$ and $\mathbb{E}\left[|Z_p^{\text{rx}}(\theta_{c,l}^{\text{rx}} + \psi(t+\tau))|^2\right] = \bar{G}_{p,c}^{\text{rx}}(t+\tau)$ are given in (12) and (13), respectively. And,

$$\mathbb{E}\left[|Z_i^{\text{tx}}(\theta_{c,l}^{\text{tx}})|^4\right]$$
$$= \int_{-\pi}^{\pi} |Z_i^{\text{tx}}(\theta)|^4 f_c^{\text{tx}}(\theta)\,d\theta, \tag{57}$$
$$\approx \frac{1}{\sqrt{\pi}} \sum_{q=1}^{N_{\text{GH}}} w_q \left| Z_i^{\text{tx}}\left(\sqrt{2}\sigma_{\text{AoD},c}x_q + \bar{\theta}_{\text{AoD},c}\right)\right|^4, \tag{58}$$

where (58) follows along lines similar to Appendix A.

Since $\alpha_{c,l}(t)\alpha_{c,l}^*(t+\tau)$ and the term $Z_p^{\text{rx}}(\theta_{c,l}^{\text{rx}} + \psi(t))\left(Z_p^{\text{rx}}(\theta_{c,l}^{\text{rx}} + \psi(t+\tau))\right)^*$ both depend on $\theta_{c,l}^{\text{rx}}$, they are correlated. Since the RVs $\bar{\alpha}_{c,l}$ and $\theta_{c,l}^{\text{rx}}$ are independent, we get

$$\mathbb{E}\left[\alpha_{c,l}(t)\alpha_{c,l}^*(t+\tau)Z_p^{\text{rx}}(\theta_{c,l}^{\text{rx}} + \psi(t))\right.$$
$$\left. \times \left(Z_p^{\text{rx}}(\theta_{c,l}^{\text{rx}} + \psi(t+\tau))\right)^*\right] = \gamma_c \Theta_c^{\text{rx}}(t,\tau), \tag{59}$$

where

$$\Theta_c^{\text{rx}}(t,\tau)$$
$$= \mathbb{E}\left[Z_p^{\text{rx}}(\theta_{c,l}^{\text{rx}} + \psi(t))\left(Z_p^{\text{rx}}(\theta_{c,l}^{\text{rx}} + \psi(t+\tau))\right)^*\right.$$
$$\times \exp\left(4\pi j t f_D \sin\left(\theta_{c,l}^{\text{rx}} + \frac{\psi(t)}{2} + \frac{\psi(t+\tau)}{2} - \theta_v\right)\right.$$
$$\times \sin\left(\frac{\psi(t+\tau) - \psi(t)}{2}\right)\right)$$
$$\left. \times \exp\left(-2\pi j \tau f_D \cos\left(\theta_{c,l}^{\text{rx}} + \psi(t+\tau) - \theta_v\right)\right)\right]. \tag{60}$$

Similarly,

$$\mathbb{E}\left[\alpha_{c,l}^*(t)\alpha_{c,l}(t+\tau)\left(Z_p^{\text{rx}}(\theta_{c,l}^{\text{rx}} + \psi(t))\right)^* \right.$$
$$\left. \times Z_p^{\text{rx}}(\theta_{c,l}^{\text{rx}} + \psi(t+\tau))\right] = \gamma_c \left(\Theta_c^{\text{rx}}(t,\tau)\right)^*. \tag{61}$$

We can simplify (60) and (61) along lines similar to Appendix A. Substituting these in (51) yields (19).

$T_{i,p}^{\text{LoS}}(t,\tau)$ consists of cross-products involving the LoS channel paths. It is given by (21). $T_{i,p}^{\text{LoS,NLoS}}(t,\tau)$ consists of cross-products involving the NLoS and LoS channel paths. It is given by

$$
\begin{aligned}
&T_{i,p}^{\text{LoS,NLoS}}(t,\tau) \\
&= \frac{K\Lambda\left|Z_i^{\text{tx}}(\theta_{\text{LoS}}^{\text{tx}})\right|^2}{L(K+1)^2}\Bigg[\left|Z_p^{\text{rx}}(\theta_{\text{LoS}}^{\text{rx}}+\psi(t+\tau))\right|^2 \\
&\quad \times \sum_{c=1}^{C}\sum_{l=1}^{L}\gamma_c\Lambda\mathbb{E}\left[\left|Z_p^{\text{rx}}(\theta_{c,l}^{\text{rx}}+\psi(t))\right|^2\right]\mathbb{E}\left[\left|Z_i^{\text{tx}}(\theta_{c,l}^{\text{tx}})\right|^2\right] \\
&\quad + \left|Z_p^{\text{rx}}(\theta_{\text{LoS}}^{\text{rx}}+\psi(t))\right|^2\sum_{c=1}^{C}\sum_{l=1}^{L}\gamma_c\Lambda\mathbb{E}\left[\left|Z_i^{\text{tx}}(\theta_{c,l}^{\text{tx}})\right|^2\right] \\
&\quad \times \mathbb{E}\left[\left|Z_p^{\text{rx}}(\theta_{c,l}^{\text{rx}}+\psi(t+\tau))\right|^2\right] \\
&\quad + 2\Re\Bigg\{\Bigg(\sum_{c=1}^{C}\sum_{l=1}^{L}\mathbb{E}\left[\alpha_{c,l}(t)\alpha_{c,l}^*(t+\tau)Z_p^{\text{rx}}(\theta_{c,l}^{\text{rx}}+\psi(t))\right. \\
&\quad \times \left.\left(Z_p^{\text{rx}}(\theta_{c,l}^{\text{rx}}+\psi(t+\tau))\right)^*\right]\mathbb{E}\left[\left|Z_i^{\text{tx}}(\theta_{c,l}^{\text{tx}})\right|^2\right]\Bigg) \\
&\quad \times \left(Z_p^{\text{rx}}(\theta_{\text{LoS}}^{\text{rx}}+\psi(t))\right)^*Z_p^{\text{rx}}(\theta_{\text{LoS}}^{\text{rx}}+\psi(t+\tau))\Bigg\}\Bigg]. \quad (62)
\end{aligned}
$$

As above, we have $\mathbb{E}\left[\left|Z_p^{\text{rx}}(\theta_{c,l}^{\text{rx}}+\psi(t))\right|^2\right] = \bar{G}_{p,c}^{\text{rx}}(t)$, $\mathbb{E}\left[\left|Z_p^{\text{rx}}(\theta_{c,l}^{\text{rx}}+\psi(t+\tau))\right|^2\right] = \bar{G}_{p,c}^{\text{rx}}(t+\tau)$, $\mathbb{E}\left[\left|Z_i^{\text{tx}}(\theta_{c,l}^{\text{tx}})\right|^2\right] = \bar{G}_{i,c}^{\text{tx}}(t,0)$, and

$$
\begin{aligned}
&\mathbb{E}\left[\alpha_{c,l}(t)\alpha_{c,l}^*(t+\tau)Z_p^{\text{rx}}(\theta_{c,l}^{\text{rx}}+\psi(t))\right. \\
&\quad \times \left.\left(Z_p^{\text{rx}}(\theta_{c,l}^{\text{rx}}+\psi(t+\tau))\right)^*\right] = \gamma_c\Lambda\Theta_c^{\text{rx}}(t,\tau). \quad (63)
\end{aligned}
$$

Substituting these in (62) yields (22).

C. Proof of Result 1

Let Φ be a beam selection rule and let $(\hat{i},\hat{p})$ be the beam pair selected by it given $\mathbf{g}$. Then,

$$
\bar{R} = \mathbb{E}_{\mathbf{g},g_{\hat{i},\hat{p}}(t_k)}\left[\frac{1}{N}\sum_{k=1}^{N}R\left(g_{\hat{i},\hat{p}}(t_k)\right)\right], \quad (64)
$$

$$
= \mathbb{E}_{\mathbf{g}}\left[\frac{1}{N}\sum_{k=1}^{N}\mathbb{E}_{g_{\hat{i},\hat{p}}(t_k)}\left[R\left(g_{\hat{i},\hat{p}}(t_k)\right)\Big|\mathbf{g}\right]\right]. \quad (65)
$$

Consider the following beam selection rule Φ^* as per which the selected beam (i^*,p^*) is

$$
(i^*,p^*) = \underset{i\in\mathcal{B}_{\text{BS}},p\in\mathcal{B}_{\text{UE}}}{\arg\max}\left\{\frac{1}{N}\sum_{k=1}^{N}\mathbb{E}_{g_{\hat{i},\hat{p}}(t_k)}\left[R\left(g_{\hat{i},\hat{p}}(t_k)\right)\Big|\mathbf{g}\right]\right\}. \quad (66)
$$

It is clear from (66) that $\sum_{k=1}^{N}\mathbb{E}_{g_{\hat{i},\hat{p}}(t_k)}\left[R\left(g_{\hat{i},\hat{p}}(t_k)\right)\Big|\mathbf{g}\right] \leq \sum_{k=1}^{N}\mathbb{E}_{g_{i^*,p^*}(t_k)}\left[R\left(g_{i^*,p^*}(t_k)\right)\Big|\mathbf{g}\right]$. Furthermore,

$$
\begin{aligned}
&\sum_{k=1}^{N}\mathbb{E}_{g_{i^*,p^*}(t_k)}\left[R\left(g_{i^*,p^*}(t_k)\right)\Big|\mathbf{g}\right] \\
&= \sum_{k=1}^{N}\mathbb{E}_{g_{i^*,p^*}(t_k)}\left[R\left(g_{i^*,p^*}(t_k)\right)\Big|g_{i^*,p^*}(T_{i,p})\right], \quad (67)
\end{aligned}
$$

because the measurements of different beam pairs are independent. Therefore, taking expectation on both sides, we get $\bar{R} \leq R^*$, where R^* is the average rate of Φ^*. Hence, (66) is the optimal beam pair selection rule.

REFERENCES

[1] T. S. Rappaport *et al.*, "Millimeter wave mobile communications for 5G cellular: It will work!," *IEEE Access*, vol. 1, pp. 335–349, May 2013.

[2] S. Rangan, T. S. Rappaport, and E. Erkip, "Millimeter-wave cellular wireless networks: Potentials and challenges," *Proc. IEEE*, vol. 102, no. 3, pp. 366–385, Mar. 2014.

[3] R. W. Heath, N. Gonzalez-Prelcic, S. Rangan, W. Roh, and A. M. Sayeed, "An overview of signal processing techniques for millimeter wave MIMO systems," *IEEE J. Sel. Topics Signal Process.*, vol. 10, no. 3, pp. 436–453, Apr. 2016.

[4] M. Marcus and B. Pattan, "Millimeter wave propagation: Spectrum management implications," *IEEE Microw. Mag.*, vol. 6, no. 2, pp. 54–62, Jun. 2005.

[5] W. Roh *et al.*, "Millimeter-wave beamforming as an enabling technology for 5G cellular communications: Theoretical feasibility and prototype results," *IEEE Commun. Mag.*, vol. 52, no. 2, pp. 106–113, Feb. 2014.

[6] M. Giordani, M. Polese, A. Roy, D. Castor, and M. Zorzi, "A tutorial on beam management for 3GPP NR at mmWave frequencies," *IEEE Commun. Surveys Tuts.*, vol. 21, no. 1, pp. 173–196, 1st Quart., 2019.

[7] *NR—Physical Channels and Modulation*, document TS 38.211, 3rd Generation Partnership Project (3GPP), V15.6.0, 2019.

[8] *NR—Physical Layer Procedures for Control*, document TS 38.213, 3rd Generation Partnership Project (3GPP), v15.6.0, 2019.

[9] D.-S. Shim, C.-K. Yang, J. Kim, J. Han, and Y. Cho, "Application of motion sensors for beam-tracking of mobile stations in mmWave communication systems," *Sensors*, vol. 14, no. 10, pp. 19622–19638, Oct. 2014.

[10] A. K. R. Chavva, S. Khunteta, C. Lim, Y. Lee, J. Kim, and Y. Rashid, "Sensor intelligence based beam tracking for 5G mmwave systems: A practical approach," in *Proc. Globecom*, Dec. 2019, pp. 1–6.

[11] Z. Qi and W. Liu, "Three-dimensional millimetre-wave beam tracking based on smart phone sensor measurements and direction of arrival/time of arrival estimation for 5G networks," *IET Microw., Antennas Propag.*, vol. 12, no. 3, pp. 271–279, Jan. 2018.

[12] J. Arnold, L. Simić, and P. Mähönen, "Experimental feasibility study of motion sensor-aided mm-wave beam tracking," in *Proc. ACM Workshop Millimeter-Wave Netw. Sens. Syst.*, Oct. 2017, pp. 5–10.

[13] Y. M. Tsang and A. S. Y. Poon, "Detecting human blockage and device movement in mmWave communication system," in *Proc.Globecom*, Dec. 2011, pp. 1–6.

[14] C. Jeong, J. Park, and H. Yu, "Random access in millimeter-wave beamforming cellular networks: Issues and approaches," *IEEE Commun. Mag.*, vol. 53, no. 1, pp. 180–185, Jan. 2015.

[15] L. Wei, Q. Li, and G. Wu, "Exhaustive, iterative and hybrid initial access techniques in mmWave communications," in *Proc. WCNC*, Mar. 2017, pp. 1–6.

[16] M. Giordani, M. Mezzavilla, C. N. Barati, S. Rangan, and M. Zorzi, "Comparative analysis of initial access techniques in 5G mmWave cellular networks," in *Proc. CISS*, Mar. 2016, pp. 268–273.

[17] Y.-N.-R. Li, B. Gao, X. Zhang, and K. Huang, "Beam management in millimeter-wave communications for 5G and beyond," *IEEE Access*, vol. 8, pp. 13282–13293, Jan. 2020.

[18] K. Gao *et al.*, "Beampattern-based tracking for millimeter wave communication systems," in *Proc. Globecom*, Dec. 2016, pp. 1–6.

[19] J. P. Nair *et al.*, "Capacity based efficient beam-selection methods for mmWave 5G MIMO communication systems," in *Proc. ICC*, May 2018, pp. 1–7.

[20] X. Gao, L. Dai, Z. Chen, Z. Wang, and Z. Zhang, "Near-optimal beam selection for beamspace mmWave massive MIMO systems," *IEEE Commun. Lett.*, vol. 20, no. 5, pp. 1054–1057, May 2016.

[21] G. E. Garcia, N. Garcia, G. Seco-Granados, E. Karipidis, and H. Wymeersch, "Fast in-band position-aided beam selection in millimeter-wave MIMO," *IEEE Access*, vol. 7, pp. 142325–142338, Sep. 2019.

[22] D. Zhang *et al.*, "Beam allocation for millimeter-wave MIMO tracking systems," *IEEE Trans. Veh. Technol.*, vol. 69, no. 2, pp. 1595–1611, Feb. 2020.

[23] H. Lee, S. Kim, and J. Choi, "Efficient channel AoD/AoA estimation using widebeams for millimeter wave MIMO systems," in *Proc. SPAWC*, Jul. 2019, pp. 1–5.

[24] M. B. Booth, V. Suresh, N. Michelusi, and D. J. Love, "Multi-armed bandit beam alignment and tracking for mobile millimeter wave communications," *IEEE Commun. Lett.*, vol. 23, no. 7, pp. 1244–1248, Jul. 2019.

[25] V. Va, T. Shimizu, G. Bansal, and R. W. Heath, "Online learning for position-aided millimeter wave beam training," *IEEE Access*, vol. 7, pp. 30507–30526, Mar. 2019.

[26] M. Polese, M. Giordani, M. Mezzavilla, S. Rangan, and M. Zorzi, "Improved handover through dual connectivity in 5G mmWave mobile networks," *IEEE J. Sel. Areas Commun.*, vol. 35, no. 9, pp. 2069–2084, Sep. 2017.

[27] *Study on Channel Model for Frequencies From 0.5 to 100 GHz*, document TR 38.901, 3rd Generation Partnership Project (3GPP), v14.2.2, 2017.

[28] M. R. Akdeniz *et al.*, "Millimeter wave channel modeling and cellular capacity evaluation," *IEEE J. Sel. Areas Commun.*, vol. 32, no. 6, pp. 1164–1179, Jun. 2014.

[29] I. A. Hemadeh, K. Satyanarayana, M. El-Hajjar, and L. Hanzo, "Millimeter-wave communications: Physical channel models, design considerations, antenna constructions, and link-budget," *IEEE Commun. Surveys Tuts.*, vol. 20, no. 2, pp. 870–913, 2nd Quart., 2018.

[30] M. Simon and M. S. Alouini, *Digital Communication Over Fading Channels*, 2nd ed. Hoboken, NJ, USA: Wiley, 2005.

[31] M. Polese and M. Zorzi, "Impact of channel models on the end-to-end performance of mmWave cellular networks," in *Proc. SPAWC*, Jun. 2018, pp. 1–5.

[32] J. G. Andrews, T. Bai, M. N. Kulkarni, A. Alkhateeb, A. K. Gupta, and R. W. Heath, "Modeling and analyzing millimeter wave cellular systems," *IEEE Trans. Commun.*, vol. 65, no. 1, pp. 403–430, Jan. 2017.

[33] M. Hashemi, A. Sabharwal, C. E. Koksal, and N. B. Shroff, "Efficient beam alignment in millimeter wave systems using contextual bandits," in *Proc. IEEE Conf. Comput. Commun. (INFOCOM)*, Apr. 2018, pp. 2393–2401.

[34] M. Nakagami, "The m-distribution—A general formula of intensity distribution of rapid fading," in *Statistical Methods in Radio Wave Propagation*, W. Hoffman, Ed. New York, NY, USA: Pergamon, Jun. 1960, pp. 3–36.

[35] M. Abramowitz and I. Stegun, *Handbook of Mathematical Functions With Formulas, Graphs, and Mathematical Tables*, 9th ed. New York, NY, USA: Dover, 1972.

[36] J. Cheng and N. C. Beaulieu, "Maximum-likelihood based estimation of the Nakagami-m parameter," *IEEE Commun. Lett.*, vol. 5, no. 3, pp. 101–103, Mar. 2001.

[37] L. S. Gradshteyn and L. M. Ryzhik, *Tables of Integrals, Series and Products*, 7th ed. New York, NY, USA: Academic, 2007.

[38] STMicroelectronics. (2017). *iNEMO Inertial Module: Always-on 3D Accelerometer and 3D Gyroscope*, DocID028475 Rev 7. [Online]. Available: https://www.st.com/resource/en/datasheet/lsm6dsl.pdf

[39] C. Tepedelenlioglu, A. Abdi, G. B. Giannakis, and M. Kaveh, "Estimation of Doppler spread and signal strength in mobile communications with applications to handoff and adaptive transmission," *Wireless Commun. Mobile Comput.*, vol. 1, no. 2, pp. 221–242, Apr. 2001.

Ashok Kumar Reddy Chavva (Senior Member, IEEE) received the Bachelor of Technology degree in electronics and communications engineering from Jawaharlal Nehru Technological University, Hyderabad, India, in 2003, and the M.E. degree in telecommunication engineering from the Indian Institute of Science, Bengaluru, India, in 2005, where he is currently pursuing the Ph.D. degree in electrical communication engineering. He joined a wireless startup, Beceem Communications, in June 2005, which later became part of Broadcom. He was involved in developing physical layer algorithms for the first 4G system based on WiMAX and LTE. He worked with Broadcom till November 2013. Since November 2013, he has been with Samsung Research and Development Institute India, Bengaluru, where he currently leads a Research and Development Team that works on differentiating solutions for mobile devices. His research interests include algorithm design for physical layer, performance evaluation of wireless communication systems, 5G NR systems, millimeter-wave and tera-hertz systems, and machine learning for communications. He received the Best Paper Award at IEEE CCNC, Las Vegas, USA, in 2016, and the Best Paper (third) at IEEE World 5G Forum, in 2020.

Neelesh B. Mehta (Fellow, IEEE) received the Bachelor of Technology degree in electronics and communications engineering from the Indian Institute of Technology (IIT) Madras in 1996, and the M.S. and Ph.D. degrees in electrical engineering from the California Institute of Technology, Pasadena, CA, USA, in 1997 and 2001, respectively. He is currently a Professor with the Department of Electrical Communication Engineering, Indian Institute of Science, Bengaluru. He is a fellow of the Indian National Academy of Engineering (INAE), the Indian National Science Academy (INSA), and the National Academy of Sciences India (NASI). He was a recipient of the Shanti Swarup Bhatnagar Award 2017 and the Swarnjayanti Fellowship. From 2012 to 2015, he has served on the Board of Governors of IEEE ComSoc. From 2014 to 2017, he has served on the Executive Editorial Committee of the IEEE TRANSACTIONS ON WIRELESS COMMUNICATIONS, where he served as its Chair from 2017 to 2018. He also serves on the steering committee of the journal.